remote sensing

MDPI

Article

Characteristics of R2019 Processing of MODIS Sea Surface Temperature at High Latitudes

Chong Jia *, Peter J. Minnett and Malgorzata Szczodrak

Department of Ocean Sciences, Rosenstiel School of Marine, Atmospheric, and Earth Science, University of Miami, 4600 Rickenbacker Causeway, Miami, FL 33149, USA; pminnett@earth.miami.edu (P.J.M.); gszczodrak@earth.miami.edu (M.S.)

* Correspondence: chong.jia@earth.miami.edu

Abstract: Satellite remote sensing is the best way to derive sea surface skin temperature (SST_{skin}) in the Arctic. However, as surface temperature retrieval algorithms in the infrared (IR) part of the electromagnetic spectrum are designed to compensate for atmospheric effects mainly due to water vapor, MODIS SST_{skin} retrievals have larger uncertainties at high latitudes where the atmosphere is very dry and cold, which is an extreme in the distribution of global conditions. MODIS R2019 SST_{skin} fields are currently derived using latitudinally and monthly dependent algorithm coefficients, including an additional band above 60°N to better represent the effects of Arctic atmospheres. However, the R2019 processing of MODIS SST_{skin} still has some unrevealed error characteristics. This study uses 21 years (2002–2022) of collocated, simultaneous satellite brightness temperature (BT) data from Aqua MODIS and in situ buoy-measured subsurface temperature data from iQuam for validation. Unlike elsewhere over the oceans, the 11 μm and 12 μm BT differences are poorly related to the column water vapor at high latitudes, resulting in poor atmospheric water vapor correction. Anomalous BT difference signals are identified, caused by the temperature and humidity inversions in the lower troposphere, which are especially significant during the summer. Although the existence of negative BT differences is physically reasonable, this makes the retrieval algorithm lose its effectiveness. Moreover, the statistics of the MODIS SST_{skin} data when compared with the iQuam buoy temperature data show large differences (in terms of mean and standard deviation) for the matchups at the Northern Atlantic and Pacific sides of the Arctic due to the disparity of in situ measurements and distinct surface and vertical atmospheric conditions. Therefore, it is necessary to further improve the retrieval algorithms to obtain more accurate MODIS SST_{skin} data to study surface ocean processes and climate change in the Arctic.

Keywords: MODIS; sea surface temperature; error characteristics; algorithm; atmospheric inversions; Arctic

check for updates

Citation: Jia, C.; Minnett, P.J.; Szczodrak, M. Characteristics of R2019 Processing of MODIS Sea Surface Temperature at High Latitudes. *Remote Sens.* **2024**, *16*, 4102. https://doi.org/10.3390/rs16214102

Received: 3 September 2024
Revised: 7 October 2024
Accepted: 29 October 2024
Published: 2 November 2024

Copyright: © 2024 by the authors. Licensee MDPI, Basel, Switzerland. This article is an open access article distributed under the terms and conditions of the Creative Commons Attribution (CC BY) license (https://creativecommons.org/licenses/by/4.0/).

1. Introduction

Sea surface temperature (SST) is a critical parameter in understanding the Earth's climate system [1,2], influencing atmospheric circulation [3,4], weather patterns [5–7], and marine ecosystems [8,9]. The accurate determination and long-term monitoring of SST are essential for climate research, oceanography, and operational meteorology. The northern high latitudes, encompassing the Arctic Ocean and its marginal seas, are regions of particular interest due to their sensitivity to climate change. This area has experienced rapid warming, with significant effects on the extent of sea ice, ocean circulation, and global climate feedback mechanisms. The precise monitoring of SST in these regions is crucial for understanding and predicting changes in the Arctic environment and for assessing their global impacts. Warming in the Arctic is occurring at more than twice the global average rate [10–12], a phenomenon known as Arctic Amplification [13,14], which underscores the urgency of accurate SST monitoring.

Infrared (IR) satellite remote sensing has emerged as a vital tool for obtaining high-resolution, global SST data, offering advantages in spatial and temporal coverage that are unattainable through in situ methods alone. Since high latitudes are beyond the geographical range of imagers on geostationary satellites, those on polar orbiters must be used, and the convergence of their subsatellite tracks in the Arctic improves the temporal sampling compared to that at lower latitudes. Infrared satellite sensors, such as the Advanced Very-High-Resolution Radiometer (AVHRR) [15], Moderate Resolution Imaging Spectroradiometer (MODIS) [16], Sea and Land Surface Temperature Radiometer (SLSTR) [17], and Visible Infrared Imaging Radiometer Suite (VIIRS) [18], provide continuous, high-resolution SST retrievals. These sensors detect thermal IR radiation emitted by the sea surface from a very thin electromagnetic skin layer a fraction of a millimeter in depth. This is embedded in the thermal skin layer, which in nearly all cases conducts heat from beneath to the interface to support heat loss to the atmosphere, resulting in the interfacial temperature being cooler than the water temperature beneath, which is referred to as the cool skin effect (for examples, see [19,20]). The temperature within the electromagnetic skin layer is thus lower than that at a depth of 1 mm or so, and this is taken as the estimate of the skin SST (SST_{skin}) [21]. Spectral radiance measurements at multiple wavelengths allow for the derivation of SST_{skin} through well-established algorithms which identify measurements contaminated by the effects of clouds and correct for the influence of a cloud-free atmosphere. These sensors are capable of providing SST_{skin} data with a spatial resolution ranging from 1 km to 4 km, and they can achieve an accuracy of around 0.3–0.5 K. However, the retrieval of accurate SST_{skin} in the northern high latitudes presents unique challenges [22–24] compared with other areas of the global ocean, primarily resulting from the extreme environmental conditions, including the presence of sea ice, frequent cloud coverage, limited in situ validation data, and the extremely cold and dry intervening atmosphere between the sea surface and the sensor apertures [25–28]. Improving SST data quality in the Arctic region has been identified as being of high priority for SST developments in the current decade [23]. An atmospheric correction algorithm utilizing single-channel brightness temperature (BT, derived from the spectral radiance measurements) from the AVHRR was proposed by Vincent et al. [29], and this algorithm was shown to outperform the standard multi-channel algorithm in a small, confined area of the Arctic known as the North Water Polynya, located north of Baffin Bay. Jia and Minnett [27] identified the main causes of the large inaccuracies in MODIS SST_{skin} retrievals in the Arctic region and developed an improved atmospheric correction algorithm based on the error characterization. Particularly, Jia and Minnett [27] demonstrated that the sea surface emissivity effect could be dominant in the inaccuracies of MODIS-retrieved SST_{skin} products and introduced an index, Emissivity-introduced BT Difference (EΔBT), to correct this emissivity effect. However, there are some remaining outliers that are not improved by corrections, indicating that MODIS SST_{skin} retrieval at high latitudes still has much room for improvement. Furthermore, Jia and Minnett [27] analyzed the R2014 SST_{skin} data rather than the R2019 products, which form the latest reprocessing of MODIS SST_{skin} retrievals with some improvements (presented in Section 2) upon the previous version. Hence, it is necessary to revisit the Arctic SST_{skin} data derived using the measurements from MODIS for a deeper insight into their error characteristics, leading to the further refinement of the atmospheric correction algorithm.

In recent years, sea ice has significantly melted and its extent has decreased due to Arctic Amplification, resulting in the opportunity to deploy more in situ instruments. The 3rd Multi-sensor Improved Sea-Surface Temperature (MISST-3) project [30] started in 2018 with the aim to continue the Group for High-Resolution Sea Surface Temperature (GHRSST) partnership and improve Arctic SST data. Saildrone unmanned surface vehicles (USVs) were deployed at the Pacific side of the Arctic in 2019, 2021, and 2022, carrying comprehensive scientific instruments for oceanography and meteorology, including CTDs to provide high-accuracy subsurface SSTs. The USV vehicles used in 2019 and 2022 were equipped with seven additional temperature loggers to measure subsurface SSTs at various depths along the keel down to 1.71 m in depth. The two Saildrones deployed in 2019

also had two IR pyrometers for the determination of SST_{skin}. These SST data are not only beneficial for the study of the thermal structure of the upper ocean [31,32] but also for validating satellite-derived SST_{skin} fields at high latitudes. Jia, et al. [33] reported the error characteristics of R2019 MODIS-retrieved SST_{skin} at northern high latitudes in comparison with the SST_{skin} derived using measurements from the two Saildrone USVs deployed in 2019 [34]. However, as a result of the limited time and space coverage of the Saildrone cruises, the number of matched MODIS–Saildrone SST_{skin} records in the dataset is relatively small and is insufficient to draw conclusions that reflect larger spatial and temporal scales. To study the characteristics in a wider range of the Arctic, this investigation uses collocated, simultaneous SST_{skin} retrievals from MODIS and in situ subsurface SST measured by buoys north of 60°N for an accuracy assessment of the MODIS retrievals. Based on the establishment of matchup data, some new findings beyond those of Jia and Minnett [27] are presented here.

This paper is organized as follows. Section 2 introduces the evolution of the atmospheric correction and cloud-screening algorithm for MODIS SST_{skin} retrieval. Section 3 provides descriptions of the datasets and methodologies used in this study. Section 4 presents the analytical results of the MODIS SST_{skin} accuracy resulting from R2019 processing, including both the similarities to and differences from the R2014 version. Section 5 discusses the results and analyzes the main causes of the two features identified in the R2019 fields. Section 6 summarizes the work and provides some suggestions for future research.

2. Background

The MODIS is an advanced remote sensing instrument that was launched aboard NASA's Terra and Aqua Earth Observing System (EOS) satellites in 1999 and 2002, viewing the entire Earth every 1 or 2 days and acquiring data in 36 spectral bands, which facilitates a deeper understanding of the global climate and processes occurring on the land [35,36], in the oceans [37,38], and in the atmosphere [39,40]. The spatial resolution of the IR bands is 1 km at nadir. The MODIS includes two mid-IR channels in the atmospheric transmission window with wavelengths close to 4 μm plus two with wavelengths centered at 10.8 μm and 12.0 μm, the traditional "split window" pair, which can be used to retrieve SST_{skin}.

This paper focuses on the currently available R2019 SST_{skin} products (https://oceancolor.gsfc.nasa.gov/resources/atbd/sst/, accessed on 2 September 2024). Public releases of SST_{skin} products prior to R2019 are no longer generated and these earlier collections are discussed here as they can provide historical context. For early versions of MODIS SST_{skin} prior to R2014, the previous version of the current release, the functional form of the SST_{skin} algorithm using the 11 μm and 12 μm longwave IR bands was the heritage AVHRR Pathfinder algorithm [41] developed by the University of Miami and used to produce a 40-year SST record based on the NOAA's AVHRR data. The Pathfinder SST_{skin} algorithm was derived from the split window non-linear SST (NLSST) algorithm [42]:

$$SST_{sat} = a_0 + a_1 BT_{11} + a_2 (BT_{11} - BT_{12}) T_{sfc} + a_3 (\sec\theta - 1)(BT_{11} - BT_{12}) \quad (1)$$

where SST_{sat} is the satellite-derived SST_{skin}, BT_{11} and BT_{12} are the BTs in the 11 μm and 12 μm wavelength bands, T_{sfc} is a "first guess" estimate of the surface temperature in the area, and θ is the satellite zenith angle. Parameters a_0 through a_3 are the algorithm coefficients derived using a generalized linear model and continuously updated based on collocated in situ buoy SSTs and satellite measurements. Coefficients were determined for the two different atmospheric water vapor regimes based on the $BT_{11} - BT_{12}$ difference [41,43] on a month-of-year basis. For daytime SST_{skin} retrievals, the reference source, T_{sfc}, was historically the NOAA 0.25° daily Optimum Interpolation Sea Surface Temperature (OISST) field [1,44]. At night, for MODIS SST_{skin} retrievals, the T_{sfc} was the SST4 4 μm product if available; otherwise, the OISST reference field was used. The SST4 is unique to MODIS and

is produced at night from measurements in the 4 μm atmospheric window, with bands 22 and 23 centered at 3.96 μm and 4.05 μm, respectively:

$$SST4 = b_0 + b_1 BT_{3.9} + b_2(BT_{3.9} - BT_{4.0}) + b_3(\sec\theta - 1) \quad (2)$$

where $BT_{3.9}$ and $BT_{4.0}$ are the BTs for MODIS bands 22 and 23, respectively. b_0 through b_3 are the regression coefficients derived similarly to those in the SST_{sat} algorithm.

To extend the NLSST algorithm for enhanced performance with the improved sensor design characteristics of MODIS, three additional correction terms were added for the R2014 processing of Aqua and Terra MODIS SST_{skin}, including terms to capture both the linear and second-degree quadratic shape of differences in retrievals across the satellite zenith angle and a single term relating to mirror side correction [45]. The updated forms of the algorithms in Equations (1) and (2) are given as follows:

$$\begin{aligned} SST_{sat} = a_0 + a_1 BT_{11} + a_2(BT_{11} - BT_{12})T_{sfc} + a_3(\sec\theta - 1)(BT_{11} - BT_{12}) \\ + a_4(\text{mirror}) + a_5(\theta) + a_6\left(\theta^2\right)\# \end{aligned} \quad (3)$$

$$\begin{aligned} SST4 = b_0 + b_1 BT_{3.9} + b_2(BT_{3.9} - BT_{4.0}) + b_3(\sec\theta - 1) + b_4(\text{mirror}) \\ + b_5(\theta) + b_6\left(\theta^2\right) \end{aligned} \quad (4)$$

where mirror represents the side number (0 or 1) of the double-sided "paddle-wheel" scan mirror on MODIS [46].

In addition, the R2014 algorithms used month-of-year coefficients generated for various atmospheric regimes based on six latitude bands (with boundaries at 90°S, 40°S, 20°S, 0°, 20°N, 40°N, and 90°N). When these changes were combined with minor adjustments to quality level definitions and thresholds for some SST flags, the uncertainty is decreased by ~0.1 K and seasonal regional biases are reduced [43,45].

As the latest reprocessing of MODIS SST_{skin} retrievals, R2019 follows the algorithm forms updated in R2014 but has an additional seventh latitude band north of 60°N for the coefficient determination to improve the atmospheric corrections in the Arctic region [27]. The reference field T_{sfc} is currently the Canadian Meteorological Center (CMC) Global Foundation SST analysis [47] instead of the NOAA OISST product, owing to the degradation and calibration issues of several of the more recent AVHRR sensors incorporated in the OISST and a reduction in the in situ observations [48]. At night, T_{sfc} still uses the SST4 if possible.

Cloud detection is also a crucial step in the MODIS SST_{skin} retrieval process, as clouds can significantly contaminate the thermal IR signal used to derive the SST [49]. Thus, radiance measurements contaminated by the presence of clouds must be eliminated from the SST_{skin} retrieval process. For the R2014 version and earlier MODIS SST_{skin} products, recursive binary decision trees, known as BDtrees, were utilized for cloud identification [41,43] based on the classification algorithm of Breiman, et al. [50]. Now, the MODIS R2019 algorithms use a new cloud classification scheme [51] based on the theory of Alternating Decision trees (ADtrees) [52,53]. One advantage of ADtree classifiers is their structure, which comprises an ensemble of both weak and strong classifiers, with multiple binary decision nodes each culminating in a prediction node that holds a vote. Each vote is weighted according to the predictive power of the test, and the votes from all true nodes are then aggregated, subsequently providing an indication of the confidence level of the classification. Unlike BDtrees, ADtrees can leverage the combined vote from a set of weak prediction nodes to alter or even override the vote of a single strong prediction node, enhancing the success rate of cloud detection.

Furthermore, a daytime ice flag was implemented in MODIS R2019 SST_{skin} processing to reduce the misclassification of sea ice as open water in transition zones, using reflectance at 671 nm and 1.6 μm with thresholds determined from the spectral histograms of manually classified Sentinel-2 Multispectral Instrument (MSI) snow or ice images [54]. This test is only applied at latitudes poleward of 30° of the subsolar point since sun glint can affect

the relative magnitudes of the reflectance. Also, the minimum value of MODIS SST was adjusted to −1.8 °C (previously −2.0 °C) in R2019.

3. Materials and Methods

3.1. MODIS SST_{skin} Data

The NASA standard processing and distribution of SST_{skin} products from the MODIS sensors are now performed using software developed at the Rosenstiel School of Marine, Atmospheric, and Earth Science at the University of Miami and applied by the Ocean Biology Processing Group (OBPG) at NASA's Goddard Space Flight Center. The OBPG generates Level-2 SST_{skin} using the Multi-Sensor Level-1 to Level-2 software (l2gen). The data can be accessed through Ocean Color web provided by the Ocean Biology Distributed Active Archive Center (OB.DAAC). The Physical Oceanography Distributed Active Archive Center (PO.DAAC) distributes the MODIS SST_{skin} fields in the GHRSST L2P format [21]. Each SST_{skin} retrieval contains a numeric Quality Level (QL) assigned by running a series of tests, with QL = 0 being the best quality and QL = 4 being the worst. Note that QLs > 1 are not recommended to be used for scientific studies as they may have significant cloud contamination identified by the ADtree cloud classifier algorithm, or other problems related, for example, to sea ice or dust aerosols.

3.2. In Situ SST Data

A near-real time (NRT) system, the in situ SST Quality Monitor (iQuam), was developed at the NOAA National Environmental Satellite, Data, and Information Service (NESDIS) Center for Satellite Application and Research (STAR) to control the quality of in situ SST measurements that come from different countries, agencies, and platforms because of their importance to the validation of satellite retrievals [55]. In iQuam (https://www.star.nesdis.noaa.gov/socd/sst/iquam/, accessed on 2 September 2024), measurements are from a variety of sources including moored buoys, drifting buoys, ships, Argo floats, and Coral Reef Watch buoys. Here, the data taken by moored and drifting buoys are considered to study the characteristics of MODIS-retrieved SST_{skin} at high latitudes. Figure 1 shows the global distribution of moored and drifting buoys in June 2024. Compared to mid-latitudes, the ocean north of 60°N is poorly sampled.

3.3. Reanalysis Data

Modern-Era Retrospective analysis for Research and Applications, Version 2 (MERRA-2) [56], a global atmospheric reanalysis produced by the NASA Global Modeling and Assimilation Office (GMAO) provides useful input data for atmospheric radiative transfer simulations conducted in this study. These data are available online through the Goddard Earth Sciences (GES) Data and Information Center (DISC) beginning in 1980. The MERRA-2 is a NASA atmospheric reanalysis for the satellite era using the Goddard Earth Observing System Model, Version 5 (GEOS-5), with its Atmospheric Data Assimilation System (ADAS), Version 5.12.4. The model includes the finite-volume dynamical core of Putman and Lin [57], which uses a cubed-sphere horizontal discretization at an approximate resolution of 0.5° × 0.625° and 72 hybrid-eta levels from the surface to 0.01 hPa [56]. As the improved version of MERRA, MERRA-2 assimilates more satellite data, including the Cross-Track Infrared Sounder (CrIS) and Advanced Technology Microwave Sounder (ATMS) onboard the Suomi-NPP satellite [58,59]; the Spinning Enhanced Visible Infra-Red Imager (SEVIRI) [60] onboard the MeteoSat geostationary satellites; and other sensors. Detailed descriptions of MERRA-2 system are presented by Gelaro, et al. [56]. Table 1 summarizes the information for MERRA-2 data used in this study.

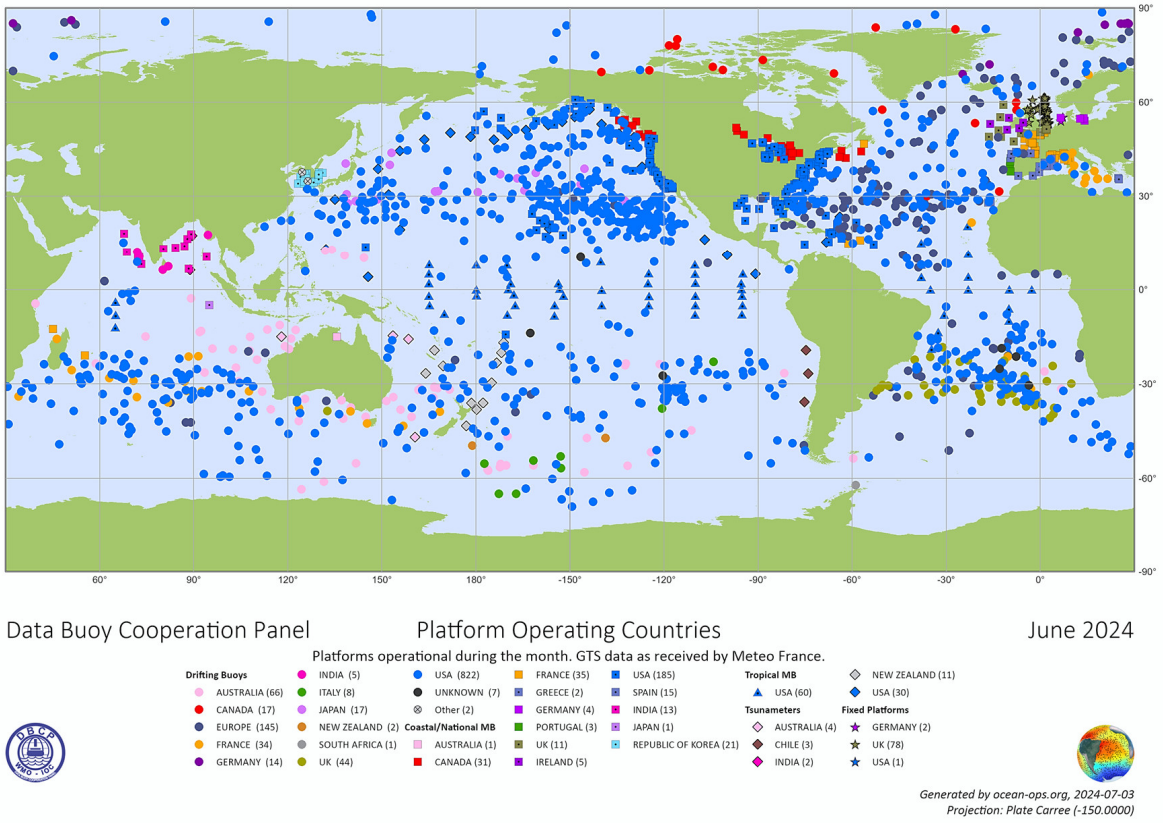


Figure 1. Distribution of global drifters, moored buoys, and some other platforms in June 2024 from https://www.ocean-ops.org/dbcp/network/maps.html (accessed on 2 September 2024).

Table 1. Details of MERRA-2 data needed for this study.

Data Name	Variables	Spatial Resolution	Temporal Resolution
inst3_3d_asm_Nv	Air temperature profile Specific humidity (water vapor) profile Pressure level	0.5° × 0.625°	3-hourly
inst1_2d_asm_Nx	2 m temperature 2 m specific humidity 2 m pressure Total precipitable water vapor		1-hourly

3.4. MODIS In Situ/Reanalysis Matchups

To generate the coefficients in the atmospheric correction algorithms (Equations (3) and (4)) and to assess the accuracy of MODIS SST_{skin} retrievals, a matchups data base (MUDB) has been established including collocated satellite and in situ observations from iQuam. Besides satellite and in situ SSTs, the MUDB also contains MODIS BTs in the relevant spectral bands, along with the time and location information for both satellite and in situ instruments and other ancillary data including viewing geometry [43]. MODIS SST_{skin} products are considered temporally coincident if the satellite measurements occurred within ±30 min of in situ observations. Spatial coincidence is evaluated with the following logic: satellite measurements are centered directly on the pixel encompassing the in situ measurement if the QL = 0 for that center pixel. However, if that pixel is not of the highest quality, then the satellite measurement is selected to be the closest highest-quality pixel that can be found within a 10 km radius of the in situ measurement [61]. Here, the MUDB for Aqua MODIS from 2002 to 2022 is used, and in order to control the satellite data quality, only those of QL = 0 (best) and QL = 1 (good) are analyzed.

The reanalysis data from MERRA-2 are also incorporated into the MUDB. The value at the MERRA-2 grid point nearest to the MODIS pixel is assigned to each matchup, which means the temporal and spatial windows are half of the resolutions of the reanalysis field needed.

4. Results

To evaluate the performance of MODIS products, we define ΔSST as the satellite-derived SST_{skin} minus its paired in situ buoy SST in the MUDB established in Section 3.4. The cool skin effect has been compensated for MODIS SST_{skin} retrievals taking account of the buoy SST measurements used to derive the algorithm coefficients, by subtracting 0.17 K from the constant terms in Equations (3) and (4). This −0.17 K value represents the empirical estimate of the average skin to sub-skin temperature difference [19]. Therefore, the MODIS-iQuam SST comparisons reported here are expected to be negative in general, which means the MODIS SST_{skin} differences relative to buoy observations should not be centered at 0 K, but should be around −0.17 K, if the atmospheric correction algorithm along with the coefficients are implemented appropriately [43].

Table 2 shows the statistics of ΔSST for Aqua MODIS from 2002 to 2022 north of 60°N. The mean and standard deviation (STD) for the QL = 0 data are −0.300 K and −0.556 K, while the mean bias is more distinct with a large variability (−0.708 K and 0.618 K) for the QL = 1 retrievals. The overall mean is −0.39 K, which is more negative than the anticipated value of −0.17 K, indicating either inadequate compensation for atmospheric effects in the retrieval algorithm or a generally stronger cool skin effect in the Arctic due to the greater heat loss from the ocean surface to the atmosphere, or both. Nevertheless, the statistical mean is significantly improved compared to the R2014 MUDB by ~0.15 K [27], demonstrating the effectiveness of adding the seventh latitude band north of 60°N for the determination and application of algorithm coefficients. Separating the MUDB into daytime and nighttime datasets, the statistics are given in Table 3. The mean biases for daytime data are less negative than those for nighttime data with slightly larger STDs, suggesting the effects of diurnal warming signals during the day. Furthermore, the number of matchups between MODIS and in situ measurements from iQuam is apparently greater in the daytime, which might be interpreted as there being more open water in the Arctic during the warmer months with longer daylight hours.

Table 2. Statistics of Aqua MODIS SST_{skin} difference compared with the buoy measured subsurface SST from iQuam from 2002 to 2022 at northern high latitudes above 60°N, including the mean, median, standard deviation (STD), and robust standard deviation (RSD; defined as the interquartile range divided by 1.35).

	Mean	Median	STD	RSD	Num
QL = 0	−0.300	−0.270	0.556	0.419	303,953
QL = 1	−0.708	−0.700	0.618	0.519	86,257
Total	−0.390	−0.345	0.595	0.478	390,210

Table 3. Similar to Table 2, but separating the daytime and nighttime data.

	Day			Night		
	QL = 0	QL = 1	Total	QL = 0	QL = 1	Total
Mean	−0.261	−0.673	−0.360	−0.358	−0.779	−0.438
Median	−0.240	−0.675	−0.325	−0.315	−0.750	−0.375
STD	0.573	0.630	0.613	0.525	0.587	0.562
RSD	0.422	0.515	0.485	0.407	0.522	0.463
Num	181,624	57,468	239,092	122,329	28,789	151,118

Figure 2a shows the time series of ΔSST with more positive outliers concentrated in the summer months due to the overwhelming diurnal warming effect on the cool skin leading

to the SST_{skin} being much warmer than the buoy-measured subsurface SST. Note that the first rapid increase in number in the MUDB is in the middle of 2007, which corresponded to the fourth International Polar Year (IPY) sponsored by the International Council for Science (ICSU) and the World Meteorological Organization (WMO) starting in March 2007, comprising an intense, coordinated field campaign of observations, research, and analysis [62]. Another peak in the data density appeared starting in 2020, which was likely associated with the COVID-19 pandemic. The COVID-19 pandemic yielded unexpected environmental benefits, as the carbon emissions in 2020 dropped by the largest amount since World War II [63]. However, the reduced human activities and associated decreases in aerosol emissions due to the lockdowns during COVID-19 are expected to have affected the climate. To be specific, a reduction in atmospheric sulphate aerosol pollutants emitted by factories, ships, and other sources decreased the amount of clouds [64] and reflected less solar radiation back to the atmosphere and space, thus resulting in a greater intensity of global warming [65] and a clearer and warmer Arctic. More clear skies permit more valid SST_{skin} data to be retrieved from MODIS IR measurements; meanwhile, anomalous surface warming could cause an early ice retreat and more open water in the Arctic [66]. Thus, the number of matchup data can be enlarged. There was a gap in data from 29 June to 5 November 2019, the cause of which has recently been identified, and this gap will be filled in a future release of the MUDB. In addition, the Aqua spacecraft transitioned to Earth Point Safe Mode on 31 March 2022, with no data being produced until 15 April 2022, when the spacecraft returned to science mode.

Figure 2b illustrates the histogram of MODIS SST_{skin} biases, which deviates from the normal distribution with negative skewness and a high kurtosis. The cold tail is much less significant than that in the R2014 MUDB [27], indicating improvements in cloud screening and atmospheric corrections for the Arctic atmospheres in R2019 processing. As shown in Figure 2c, the satellite and in situ SSTs are well correlated at warmer temperatures, but have larger discrepancies at low temperatures, especially around 0 °C. The spatial distribution of ΔSST is given in Figure 2d, in which most of the matchup data were collected in the Atlantic Sector of the Arctic and very few points were located north of 80°N because of the perennial sea ice cover. For those outliers with an absolute value > 2 K as plotted in Figure 2e, the spatial pattern is as homogeneous as shown in Figure 2d, implying that the MODIS-retrieved SST_{skin} data with large differences from the in situ observations at high latitudes do not possess evident spatial characteristics.

The MODIS-iQuam SST difference can result from the discrepancies in space and time between the MODIS pixel and in situ measurement. The sensitivity of ΔSST to the time window is weak for both the daytime and nighttime MUDB as shown in Figure 3, which means the interval of ±30 min makes negligible contributions to MODIS SST_{skin} estimates of inaccuracy. However, in contrast to the nighttime data, the daytime regression slope given in Figure 3a is significantly different from zero at a confidence level of 95%. It is likely associated with diurnal variations of the surface temperature, as has also been found by Embury, et al. [67] and Høyer, et al. [26]. According to Figure 4, the ΔSST is more sensitive to spatial separation during the day and at night. Such a negative trend is expected because when the pixel containing the position of the in situ matchup is cloudy, the nearest pixel that is determined to be cloud-free may have a higher likelihood of being contaminated by undetected clouds. The error characteristics due to the non-coincidence in space and time are similar to those in the MODIS–Saildrone SST_{skin} matchups analyzed by Jia, et al. [33].

The MODIS SST_{skin} retrieval algorithm mainly compensates for the water vapor effect in the atmospheric correction using the difference in BTs measured at 11 μm and 12 μm wavelengths, which results from the spectral dependence of the absorptivity of water vapor. However, the scatter plots in Figure 5 demonstrate the BT difference is much less correlated with the total column water vapor in the atmosphere at high latitudes, which has been presented previously [68–70] and has also been validated in the R2014 MODIS MUDB [27]. Unlike the R2014 SST_{skin} fields, the cut-off pattern of BT differences does not appear in the R2019 data, presumably due to the updated cloud classification algorithm

using ADtrees. The BDtrees applied in R2014 processing would ruthlessly reject some measurements when the BT difference is above or below specific values under certain circumstances, leading to some good-quality (cloud-free) pixels being discarded and an overly conservative cloud mask. The advantage of using a machine-learning-based ADtree classifier to detect clouds, compared to BDtrees, is that the overall misclassification rate is greatly decreased, particularly for false positive clouds, and the number of valid retrievals increases compared to R2014 [51]. A total number of 66,024 matchups, including both QL = 0 and QL = 1 data, in the R2014 Aqua MODIS MUDB from 2013 to 2017 north of 60°N were analyzed by Jia and Minnett [27], while there are 107,692 valid data points in the R2019 fields during the same period, which is an increase of ~63%. Figure 5a shows an even weaker correlation between the BT difference and atmospheric water vapor content for the daytime dataset due to the existence of some anomalous negative BT differences which are rarely observed at night, as shown in Figure 5b. The cause of these negative BT differences will be discussed in Section 5.

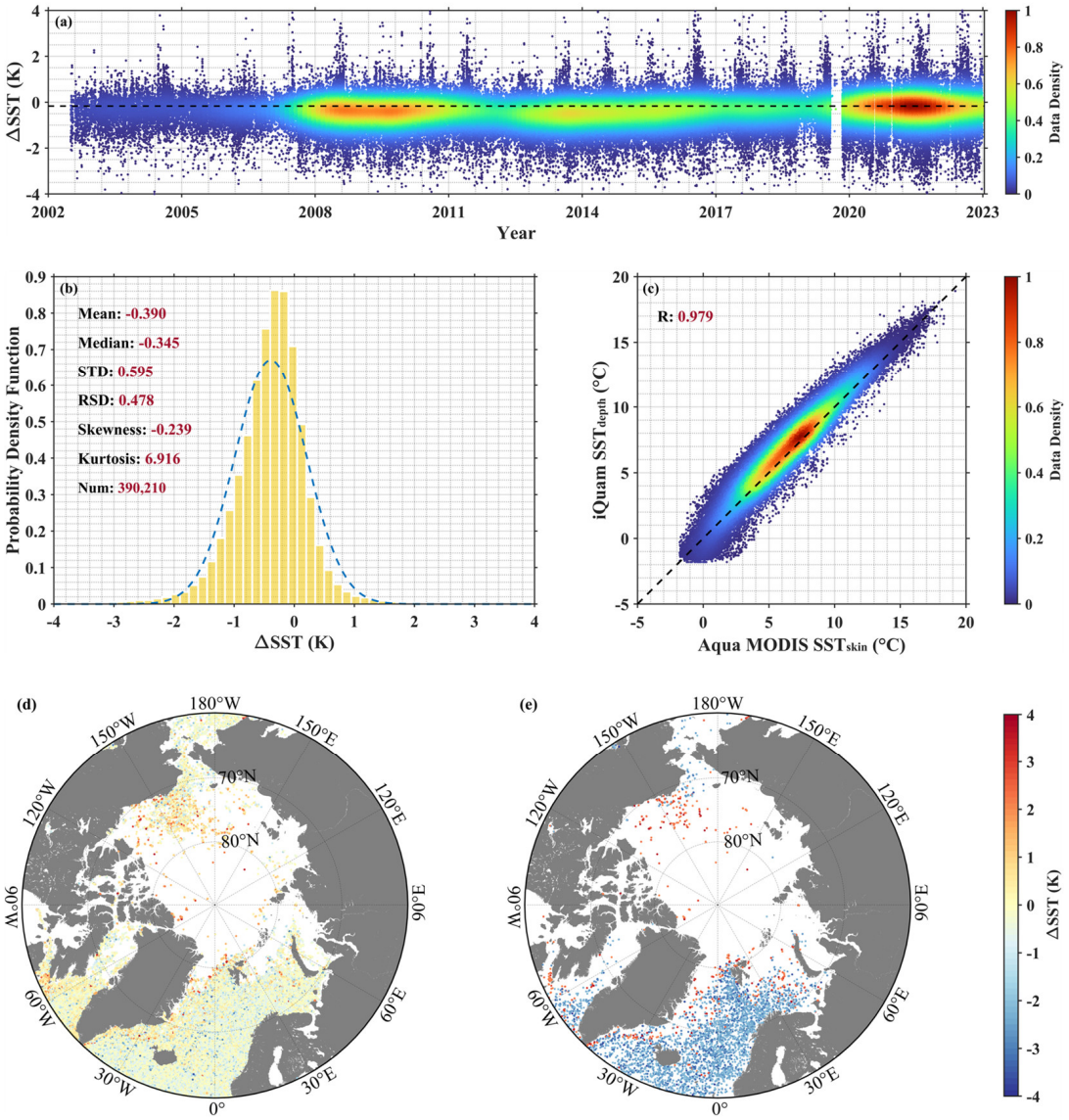


Figure 2. (**a**) Time series of the Aqua MODIS-iQuam SST difference (ΔSST) above 60°N from 2002 to 2022, including both QL = 0 and QL = 1 data. The black dashed horizontal line indicates the value of −0.17 K. (**b**) Histogram of the ΔSST with fitted normal distribution as blue dashed curve. (**c**) Scatter plot of Aqua MODIS SST_{skin} and in situ buoy SST measurements from iQuam colored according to data density. (**d**) Map of Aqua MODIS ΔSST. (**e**) Map of Aqua MODIS ΔSST > 2 K or <−2 K.

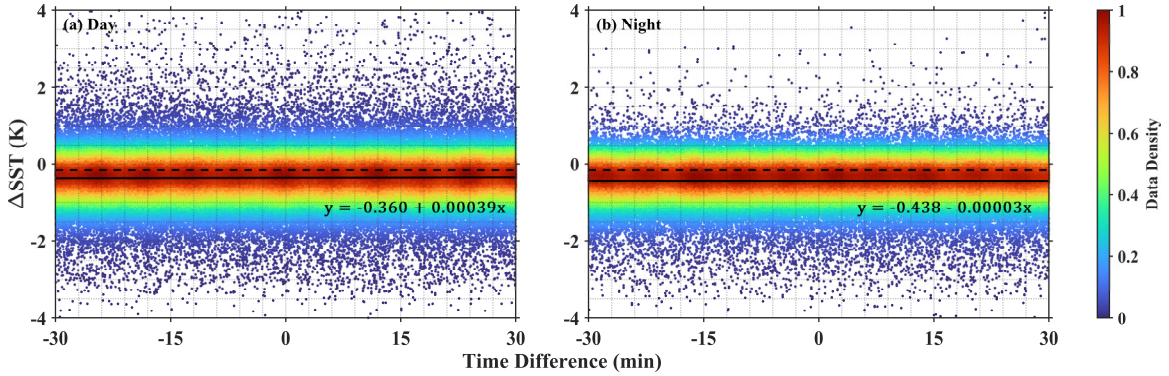


Figure 3. Aqua MODIS ΔSST as a function of time difference between the satellite and in situ buoy measurements for the (**a**) daytime and (**b**) nighttime data. The scatter plots are colored according to the data density. The dashed black horizontal lines are at −0.17 K, and the linear regressions are plotted as black solid lines with the functional expressions given in the plots.

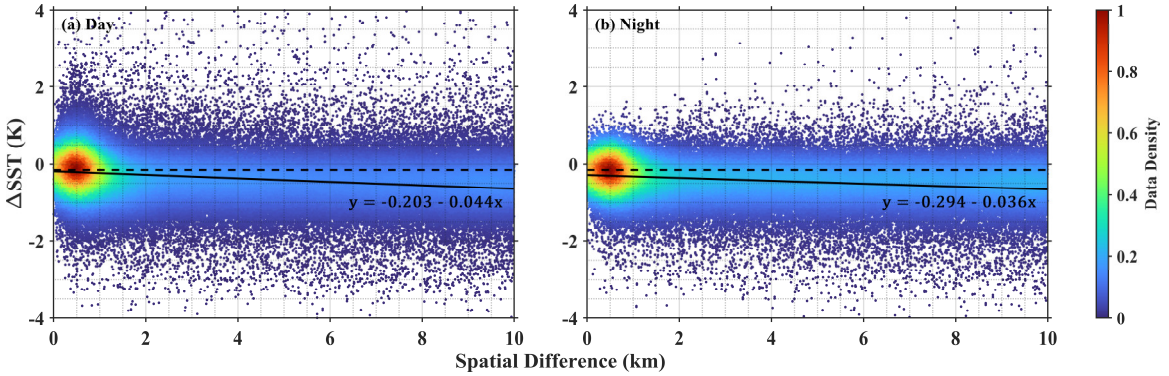


Figure 4. Similar to Figure 3, but for the Aqua MODIS ΔSST as a function of spatial distance between the satellite and in situ buoy measurements.

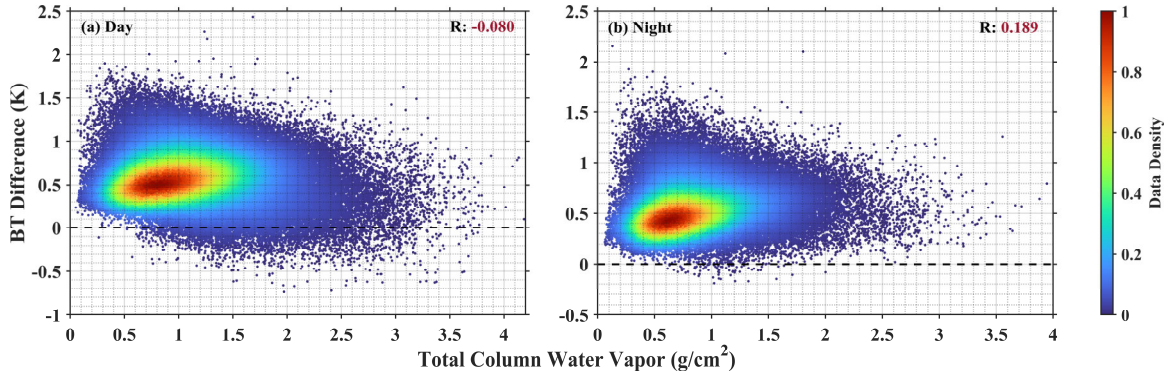


Figure 5. BT difference ($BT_{11} - BT_{12}$) as a function of total column water vapor in the MUDB during the (**a**) day and (**b**) at night. The scatter plots are colored according to data density, and the black dashed lines indicate a BT difference of zero. The correlation coefficients are also given on the upper right.

Considering that the BT differences at 11 μm and 12 μm channels are generally insufficient to represent the IR water vapor absorption in the atmospheric radiative transmission, the corrections for the atmospheric effects in the MODIS SST_{skin} retrieval algorithm are possibly inappropriate. The ΔSSTs tend to be inversely related to the BT difference for each month as shown in Figure 6a–l. Both regression slopes and intercepts possess significant and synchronous seasonal variability (Figure 6m); that is, the regression slopes are more negative during the warm months while the intercepts are less negative or even

positive. The main cause of this is the increased number of negative BT differences and the consequential large positive ΔSSTs in summer. Note that the correlation in Figure 6 is the strongest in May rather than in the warmer months, such as July or August. This may be explained by the increasing positive outliers of ΔSST due to diurnal warming for positive BT differences in summer months, which lower the slope of the linear regression.

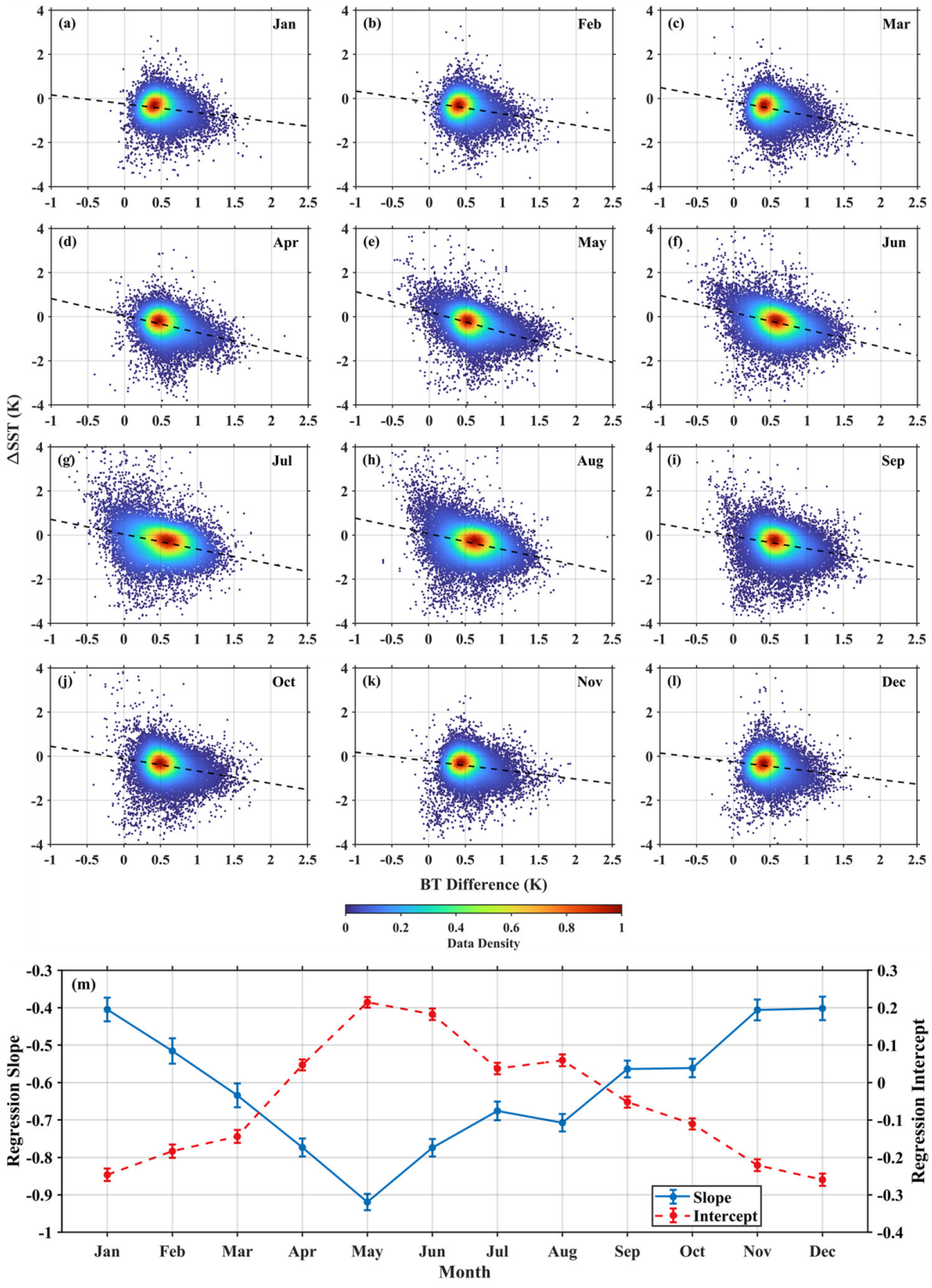


Figure 6. (**a**–**l**) Monthly scatter plots of Aqua MODIS ΔSST as a function of BT difference colored according to data density and fitted by linear regression in black dashed lines. (**m**) Monthly regression slope (blue) and intercept (red) variation, with the error bars indicating the uncertainties.

5. Discussions

5.1. Anomalous BT Differences

Some anomalous BT differences, $BT_{11} - BT_{12} < 0$, in the thermal emissive bands are observed in the R2019 MUDB at high latitudes as presented in Section 4, whereas those signals were excluded in the high-quality R2014 MUDB by the BDtree cloud masking methodology. The noise-equivalent temperature difference (NEΔT), a measure of noise in the BT measurements, is 0.02 K and 0.03 K in Band 31 at 11 μm and Band 32 at 12 μm of the Aqua MODIS sensor, as evaluated by Madhavan, et al. [71], which is well within the specification of 0.05 K. Thus, BT differences $\leq$ 0.036 K should be considered as anomalous measurements not significantly > 0 based on the propagation of uncertainty for linear combinations.

Table 4 shows the statistics of Aqua MODIS ΔSST for those BT difference anomalies. The mean and median show distinct positive biases up to ~0.4 K, far from the negative values of the metrics in the general R2019 MUDB. The STD and robust standard deviation (RSD; calculated as the interquartile range divided by 1.35) are also >1 K, indicating the failure of the atmospheric correction algorithm. North of 60°N, there are 5607 samples, ~1.4% of the total valid database, with abnormal BT differences, mostly (96.3%) occurring in the daytime. Due to the small number of samples, the extremely negative mean and median for the nighttime data given in Table 5 might not be representative. Most occurrences of BT differences $\leq$ 0.036 K are during the day as a consequence of the large increase in the number of daytime Level-2 valid retrievals (ranging between 30% and 60% throughout the year) by applying the ADtree cloud classification models in R2019 processing, whereas the increase is quite modest (ranging between 2% and 8%) at night [51]. The spatial distribution of anomalous BT difference possesses some characteristics that are different from the normal BT difference, as shown in Figure 7. The anomalous BT differences are mostly located at higher latitudes north of 70°N, and a slightly larger portion is concentrated at the Pacific side of the Arctic.

Table 4. Similar to Table 2, but only for the Aqua MODIS R2019 MUDB when the BT difference between 11 μm and 12 μm wavelengths $\leq$ 0.036 K.

	Mean	Median	STD	RSD	Num
QL = 0	0.356	0.430	1.258	1.078	4457
QL = 1	0.249	0.370	1.337	1.096	1150
Total	0.334	0.415	1.275	1.089	5607

Table 5. Similar to Table 3, but only for the Aqua MODIS R2019 MUDB when the BT difference between 11 μm and 12 μm wavelengths $\leq$ 0.036 K.

	Day			Night		
	QL = 0	QL = 1	Total	QL = 0	QL = 1	Total
Mean	0.456	0.313	0.426	−2.036	−2.285	−2.070
Median	0.478	0.400	0.460	−2.295	−2.668	−2.330
STD	1.162	1.284	1.190	1.069	0.935	1.053
RSD	1.015	1.078	1.033	1.240	0.752	1.230
Num	4278	1122	5400	179	28	207

Even though these BT difference signals can possibly be caused by cloud-contaminated pixels misclassified as clear skies, they can also be physically reasonable, especially considering most of the anomalous BT differences were taken in sunlight and the classifier success rate of ADtree is higher during the day (92.07%) than at night (89.94%) [51], as some attributes in the visible bands of MODIS were used during the training of the ADtree classification models. As for physical causes, an examination of the vertical profiles of air temperature and specific humidity in the lower troposphere (beneath 500 hPa) in the MERRA-2 reanalysis data reveals significant temperature inversion (TI; Figure 8a) and

humidity inversion (HI; Figure 8b) when abnormal BT differences were measured. In meteorology, a TI (HI) is defined as a layer in which air temperature (specific humidity) increases with height. Both TIs and HIs are common features in the Arctic throughout the year and have been investigated by many researchers [72–78]. The occurrence of Arctic TIs is usually caused by the surface radiative cooling and some synoptic-scale atmospheric flows, including warm air advection and subsidence (anticyclonic). HIs often exist simultaneously with TIs [76,79,80] but can also be related to the moisture transport from lower latitudes and the atmospheric large-scale circulation associated with the climate indices such as the Arctic Oscillation and the North Atlantic Oscillation [81,82]. Due to the larger water vapor effect at 12 μm than at 11 μm, the existence of TIs and HIs in the lower troposphere can give rise to amplified discrepancies in the emittance in these inversion layers between the two wavelengths. The greater atmospheric attenuation of surface emissions at 12 μm would be compensated for to a greater or lesser degree, resulting in the possibility of the spectral radiance received by satellite sensors at 12 μm being closer to or even greater than that at 11 μm, leading to very small positive or even negative BT differences. The anomalous BT differences were not observed in the high-quality R2014 MUDB since they were incorrectly classified as resulting from the presence of clouds by the BDtree algorithm. Such signals are rarely found at lower latitudes in the R2019 MUDB, such as the Southern Hemispheric tropics and mid-latitude regions [83], indicating that the prevalent TIs and HIs in the Arctic are the mechanisms of reducing BT differences between 11 μm and 12 μm, even leading to a reversal of the sign. The monthly distributions of air temperature profiles in Figure 9 demonstrate distinct seasonal variability, with more identified BT differences $\leq$ 0.036 K and significant TI features in warmer months from May to September. Similarly, strong HIs exist as shown in Figure 10. The BT difference anomalies are generally found in warmer and more humid Arctic air during the ice melt season with more open water north of 60°N, considering the inversion occurrence generally increase with latitude [72,78]. Also, longer daylight leads to more data being collected, in view of the better performance of the ADtree algorithm in the daytime. So, the small number of anomalous BT differences in the MUDB during winter may be influenced by the sampling limitations due to different geophysical conditions (greater sea ice coverage) and the contributions of a slightly less accurate ADtree cloud classifier scheme at night.

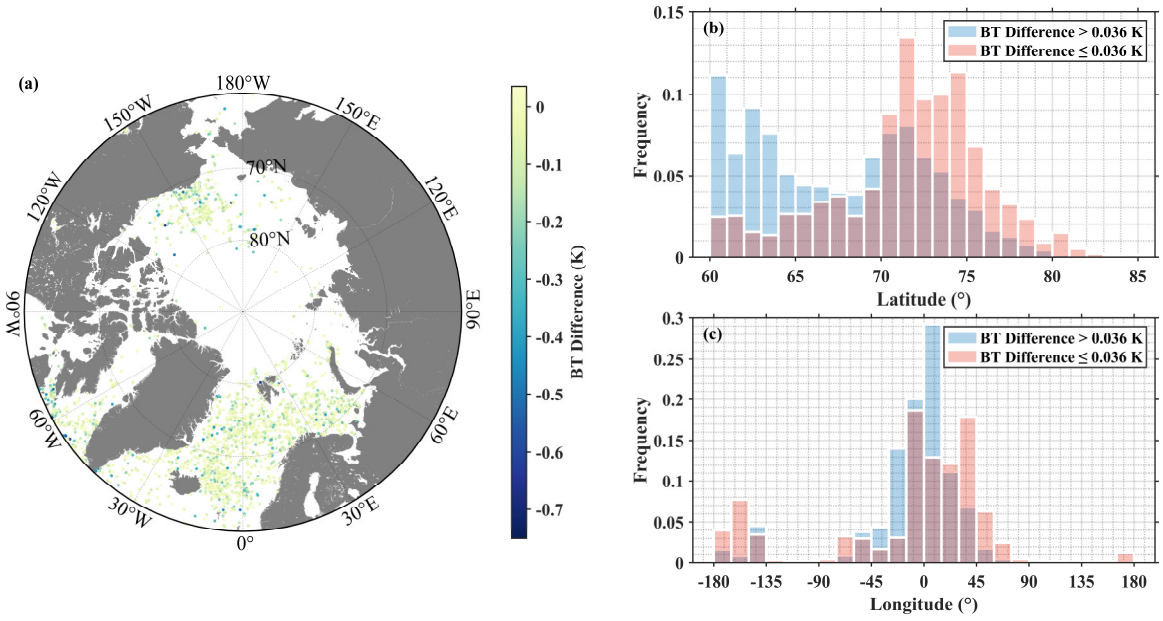


Figure 7. (**a**) Map distribution of the anomalous BT differences in the R2019 MUDB above 60°N. Histograms of (**b**) latitude and (**c**) longitude for Aqua MODIS measurements in the MUDB when the BT differences are >0.036 K (light blue) and are ≤0.036 K (light red).

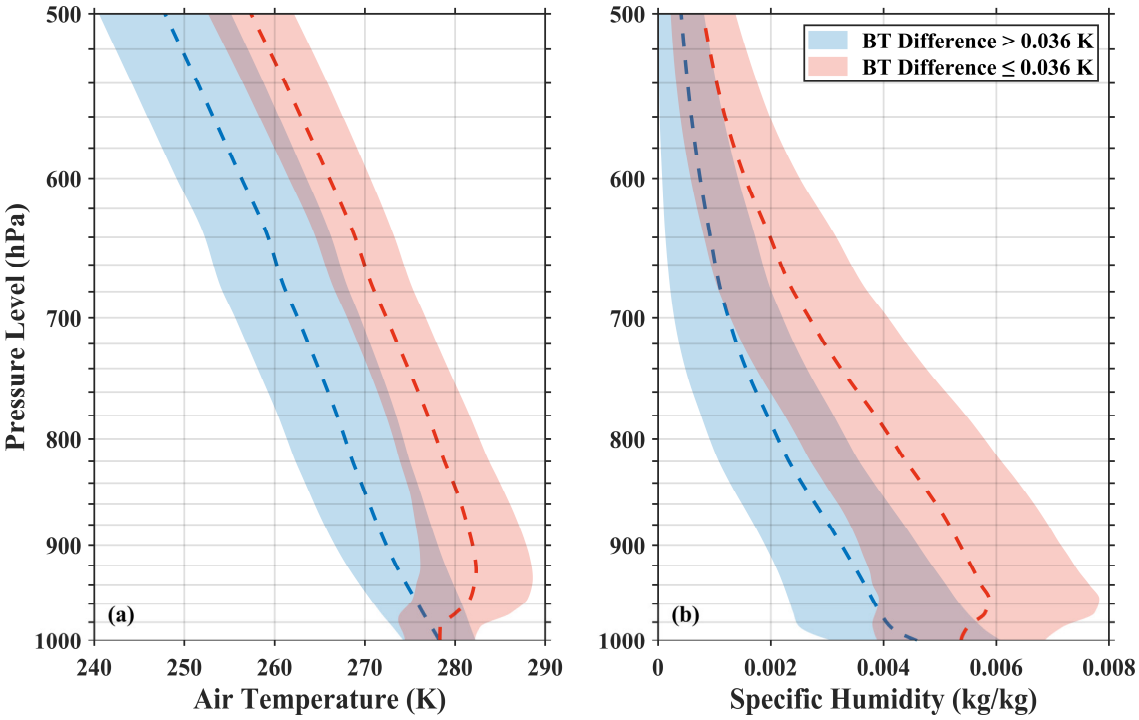


Figure 8. MERRA-2 reanalysis atmospheric profiles matched with Aqua MODIS R2019 MUDB north of 60°N including (**a**) air temperature and (**b**) specific humidity, plotted as the mean (dashed line) ± 1 STD (envelope) beneath the 500 hPa level for the measurements of BT difference > 0.036 K (blue) and BT difference ≤ 0.036 K (red).

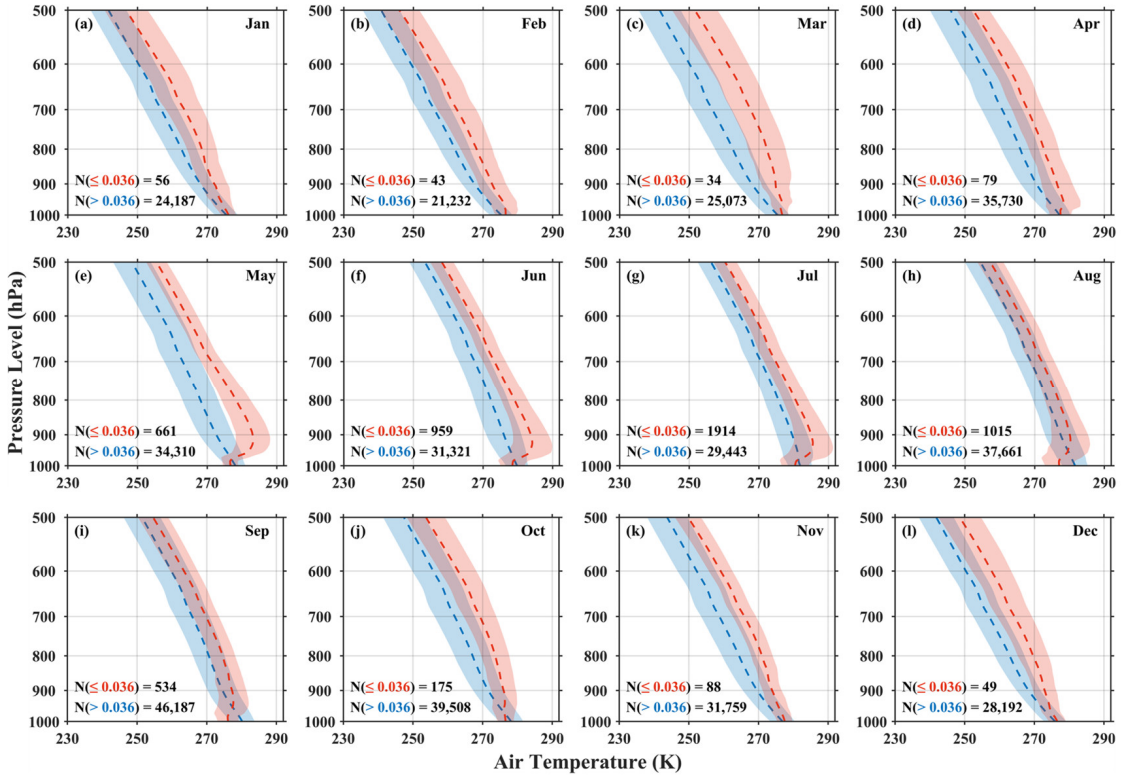


Figure 9. (**a**–**l**) Monthly distributions (mean ± 1 STD) of the MERRA-2 air temperature profiles beneath the 500 hPa level for the normal and abnormal BT difference cases. The number of data points in each dataset is given in the lower left section of each panel.

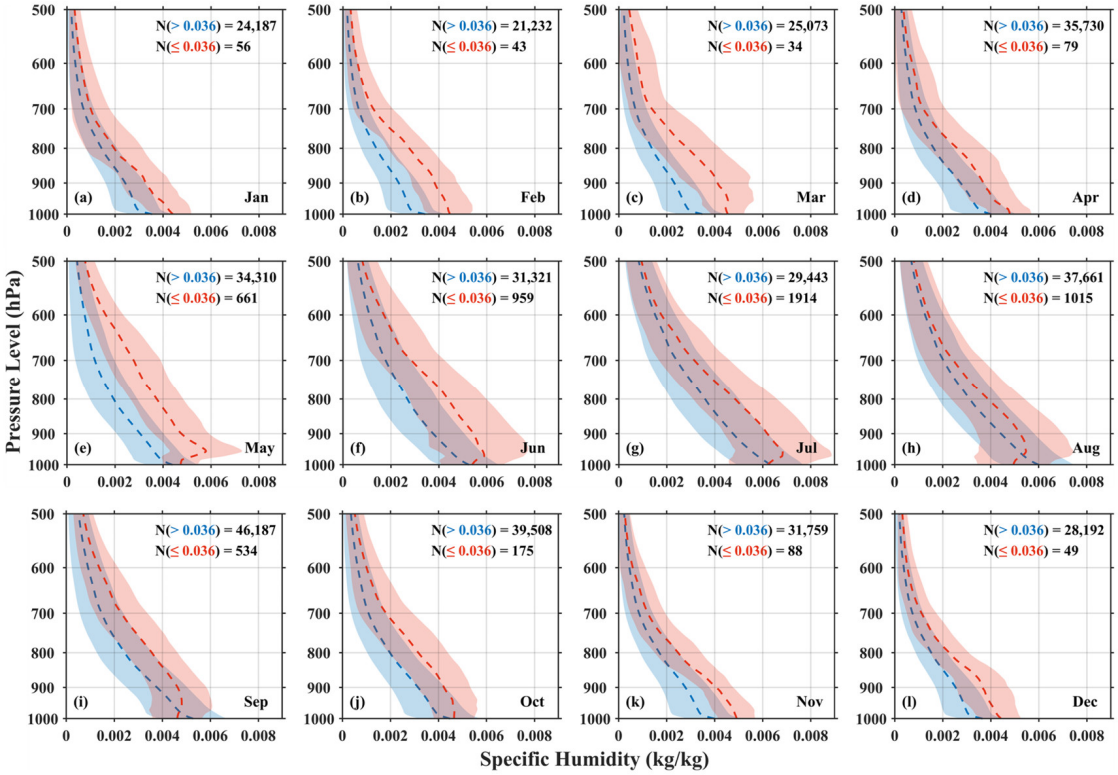


Figure 10. Similar to Figure 9a–1, but for the MERRA-2 specific humidity profiles beneath the 500 hPa level. The number of each dataset is given in the upper right section of each panel.

To quantify further the effects of the inversions on the MODIS BT differences, the frequency of occurrence and the strengths of TIs and HIs in the MUDB were examined. The frequency of occurrence is given by the percentage of the number of valid profiles showing inversions; the inversion strength is defined as the temperature/specific humidity difference between the levels in which the inversions occur. In the case of multilayer inversions, the inversion strength is the accumulation of the temperature/specific humidity differences across the inversion layers. To enhance the reliability of quantifying the occurrence of TIs and HIs, TI intensities < 0.3 K and HI intensities < 2×10^{-5} kg/kg are ignored to eliminate the effects of possibly artificial inversions resulting from inaccuracies in the MERRA-2 reanalysis data [76]. The occurrence of both TIs and HIs reaches 98% for these anomalous BT differences but is only 56%–60% for the profiles leading to normal BT differences. According to the monthly frequency distribution, both TIs and HIs occur more frequently in warmer months when the BT difference > 0.036 K, as shown in Figure 11a. However, it is worth noting that the seasonal variations are represented by the characteristics of data collected in the MUDB and may not accurately reflect the occurrences over the entire ice-free Arctic due to the uneven sampling in terms of the time and location of the matchups. The coexistence of TIs and HIs is nearly inevitable in warm seasons for these abnormalities of BT differences (Figure 11b), while some cases without either TIs or HIs are found in winter, indicating the possible failure of the ADtree cloud mask, or unrepresentative atmospheric profiles due to the low resolution of the MERRA-2 reanalysis, or other potential mechanisms for reversing the sign of the BT difference, such as aerosols. Figure 11 illustrates that the existence of TI and/or HI is necessary but not sufficient for the formation of anomalous BT differences under clear skies. Figure 12a,b confirm that the strengths of TIs and HIs for the anomalous BT differences are much greater than those for normal BT differences when inversions exist; the largest discrepancies are in summer, when there are the most anomalous BT differences. The effects of TI and HI on BT differences > 0.036 K are expected to be minor due to their relatively weak strengths. The monthly variations of BT difference with the changes in atmospheric water vapor content are still present in general as shown in Figure 12c. However, strong TI and HI conditions

can reverse the sign of BT differences and make them more negative at the higher inversion intensities. The coexistence of strong TIs and HIs results in visibly negative BT differences reaching −0.5 K (Figure 12d). HIs are usually stronger in summer due to there being more water vapor content in the atmosphere [73], which could also explain the greater occurrence of anomalous BT differences in this season.

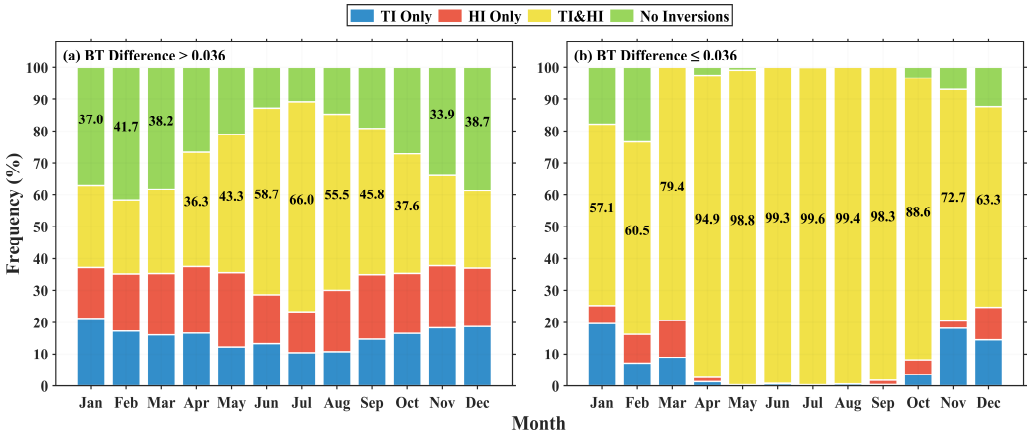


Figure 11. Monthly occurrence frequency of temperature inversion (TI) only (blue), humidity inversion (HI) only (red), simultaneous TI and HI (yellow), and neither TI nor HI (green) for (**a**) BT difference > 0.036 K and (**b**) BT difference ≤ 0.036 K. The highest frequency among the TI/HI situations in each month is shown in the corresponding part of the column.

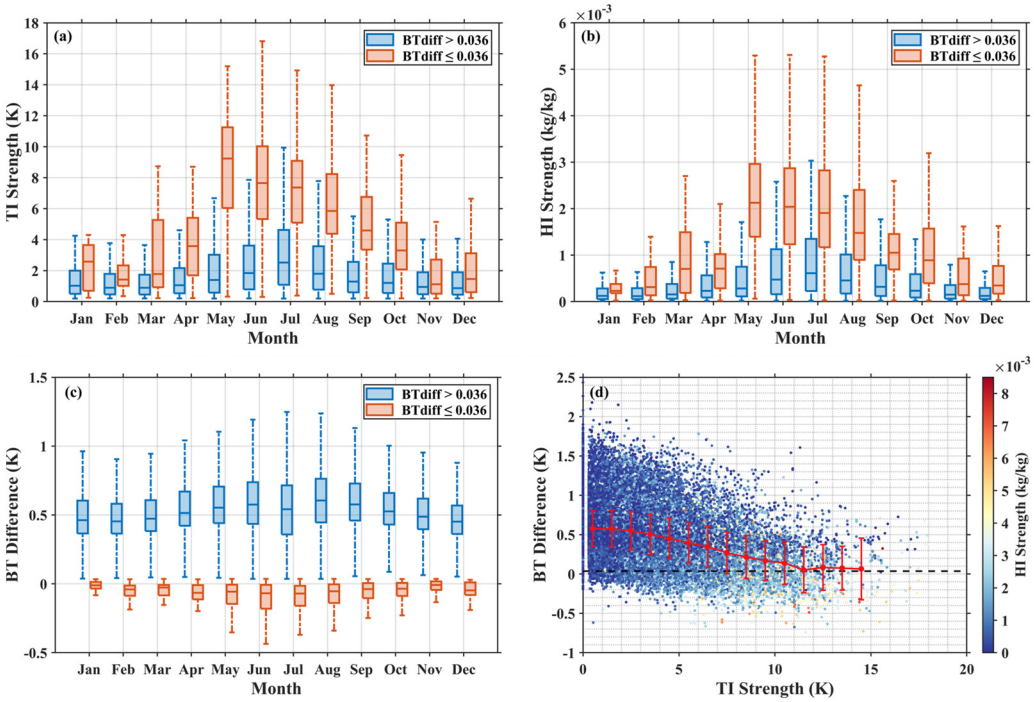


Figure 12. Monthly variations of (**a**) TI strength, (**b**) HI strength, and (**c**) BT difference between 11 μm and 12 μm for BT difference > 0.036 K (blue) and BT difference ≤ 0.036 K (red) only when TI or HI exists. For the boxplots, the ends of the boxes, the ends of the whiskers, and the line in the box represent the 25th and 75th percentiles, the minimum and maximum values that are not outliers, and the median, respectively. Outliers are values beyond 75th percentile +1.5* (interquartile range) or less than 25th percentile −1.5* (interquartile range), which are not shown here. (**d**) Scatter plot of BT difference as a function of TI strength colored according to the HI strength. The black dotted line indicates the BT difference value of 0.036 K, the threshold of positive BT differences greater than the NEΔT effects. The red dots and error bars are the mean and STD of the BT difference, calculated at 1 K intervals of TI strength.

5.2. Differences Between the Atlantic and Pacific Sectors

According to Figure 2d, the Aqua MODIS-iQuam matchup data are distributed unevenly in space, mostly concentrated in the Greenland, Norwegian, and Barents Seas at the Atlantic side of the Arctic. This is explained by the greater ice-free area throughout the year as a result of the import of warm, salty water from lower latitudes associated with the North Atlantic Current and wind-driven atmospheric circulations bringing warm air northward (e.g., controlled by the "Icelandic Low" system). Thus, the coefficients of the MODIS SST_{skin} retrieval algorithm north of 60°N are derived using data mostly from those regions in the R2019 MUDB. This then prompts the following question: how well do these coefficients represent the regions elsewhere at northern high latitudes, such as the Pacific Sector in the Arctic?

Here we define the Atlantic Sector and Pacific Sector of the Arctic as the entire region north of 60°N encompassing 30°W–30°E and 150°E–150°W, respectively. Table 6 shows the statistics of Aqua MODIS ΔSST are dissimilar in the two sectors. It is expected that the statistics at the Atlantic side are close to those for the total MUDB given in Table 2 due to the dominant weight in the number of data used to derive coefficients for the atmospheric correction algorithm. However, the MODIS SST_{skin} retrievals in the Pacific Sector have generally less negative or even positive biases from the in situ observations. The differences in the mean and STD reach up to 0.4 K and 0.3 K. As plotted in Figure 13, marked differences are present in each month (except April, which has very small differences) and are most apparent in summer, even though there are differences in the number of cases in each month and region. Due to the sea ice edge being further south during the frozen period in the Pacific Arctic, even sometimes south of 60°N, the number of data points in the R2019 MUDB is very small, with only dozens of MODIS-iQuam matchups for each month (December–May) in the past two decades. As the sea ice retreats back to the central Arctic Ocean on the Pacific side in warmer months, there can be several thousand collections, even though this is still not comparable to the numbers in the Atlantic Sector due to the scarce deployments of the in situ observation systems as shown in Figure 1.

Figures 14 and 15 illustrate the general profiles of air temperature and specific humidity in the lower troposphere distributed in the Atlantic and Pacific Sectors, as represented in the R2019 MUDB. Both parameters have significantly different vertical structures in most months. Strong TIs are found in the Pacific Arctic in February and in summertime, including in June, July, and August. For the other months, the divergence of air temperatures is also pronounced, especially at the near-surface level beneath 900 hPa. The atmosphere is generally drier at the Pacific side in the MUDB; however, the HI features are not as distinct as TIs in summer. According to Figure 16a,b, the frequencies of occurrence of TI, HI, and coexisting TI and HI are higher in the Pacific Arctic, together with the greater strengths given in Figure 16c,d. The more frequent and stronger TI and HI events in summer result in a larger fraction of anomalous BT differences $\leq$ 0.036 K, as shown in Figure 16e, consistent with the results in Section 5.1. Thus, even though the water vapor content increases in summer conditions at the Pacific side of the Arctic, as given in Figure 16f, the general BT difference decreases as a result of TIs and HIs. Despite the weak correlation between the BT difference at 11 μm and 12 μm wavelengths and the total column water vapor in the atmosphere (Figure 5), the relatively lower atmospheric water vapor content at the Pacific side of the Arctic in most months (Figure 16f) should also contribute to the generally smaller BT differences than those at the Atlantic Sector. The spatial distributions of water vapor content at the Atlantic and Pacific Sectors are significantly different throughout the year as shown in Figure 17, particularly in the winter due to most of the Pacific Arctic being covered by sea ice and there being more open water on the Atlantic side. As sea ice melts in summer, the air in the Pacific Arctic becomes more humid with rising air temperatures, leading to the total column water vapor being close to or even higher than that in the Atlantic side at the same latitude.

To summarize, the atmospheric conditions indicated by the data in the MUDB collected in the Atlantic and Pacific Sectors of the Arctic are apparently different in terms of the

vertical profiles of both temperature and humidity. More frequent and stronger TIs and HIs are found in the Pacific Arctic, particularly in the summer months. Combined with the effect of a generally lower water vapor content in the atmosphere for most of the year, the resulting MODIS BT difference measurements between 11 μm and 12 μm bands are smaller than those in the Atlantic Arctic overall or are even negative values. These anomalous BT differences $\leq$ 0.036 K compromise the atmospheric correction algorithm, resulting in the extreme statistics given in Tables 4 and 5, but given the small portion in the dataset (Atlantic: 0.9%; Pacific: 6.6%), it is not the main cause of the large statistical discrepancies between the two sectors provided in Table 6. Fundamentally, the MODIS SST_{skin} retrieval algorithm coefficients primarily derived from the matchup data at the Atlantic Sector of the Arctic are not appropriately representative of the meteorological variability at the Pacific side. The uneven latitudinal distribution of sampling is shown in Figure 18a. During frozen months, data in the Pacific side are mostly south of 65°N due to the presence of sea ice, while in summer, the matchups are concentrated around 70°N, likely due to the buoys drifting with the increased Pacific inflow through the Bering Strait to the Arctic Ocean [84]. The larger number of summer TIs and HIs thus can be explained since the inversion occurrence generally increases with latitude [72,78]. Also note that the in situ subsurface SST data sampled in the Pacific Arctic have a greater portion of low-temperature measurements (even below 0 °C; Figure 18b), indicating the proximity to the marginal ice zone where large horizontal temperature gradients might complicate the satellite in situ comparison with a larger separation. Apart from the inappropriate algorithm coefficients used for the Pacific Sector, a higher percentage of daytime data (75.8%) compared to the Atlantic side (60.3%) may also partially explain the more positive statistics of the mean and median ΔSST for Aqua MODIS as a result of more frequent diurnal warming events [32].

Table 6. Statistics for the Aqua MODIS ΔSST in the Atlantic Sector and Pacific Sector of the Arctic using the R2019 MUDB.

	Atlantic Sector (30°W–30°E)			Pacific Sector (150°E–150°W)		
	QL = 0	QL = 1	Total	QL = 0	QL = 1	Total
Mean	−0.354	−0.768	−0.446	0.065	−0.394	−0.037
Median	−0.310	−0.745	−0.385	0.058	−0.410	−0.045
STD	0.508	0.570	0.550	0.812	0.838	0.840
RSD	0.396	0.493	0.456	0.633	0.663	0.663
Num	224,508	64,315	288,823	8612	2465	11,077

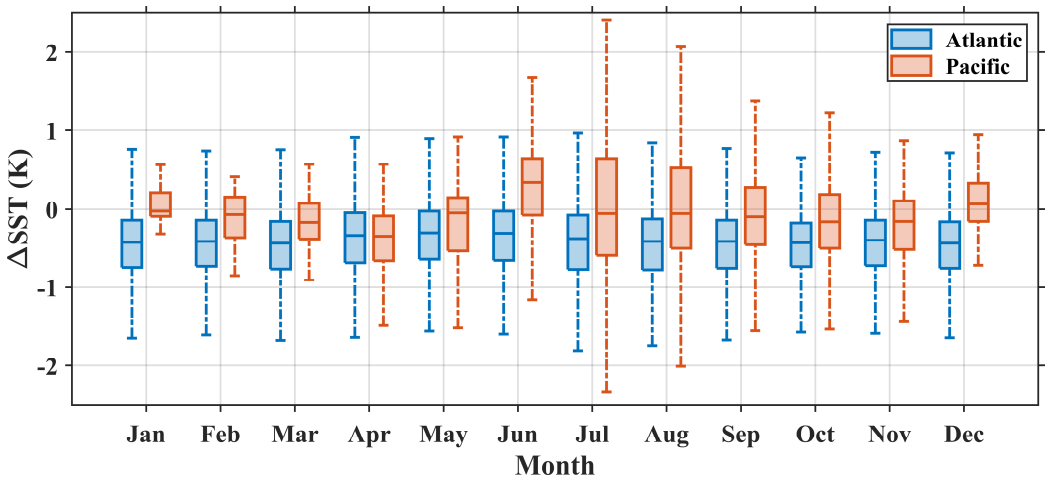


Figure 13. Monthly boxplots of the Aqua MODIS ΔSST in the Atlantic Sector (blue) and the Pacific Sector (red) of the Arctic. Outliers are not shown.

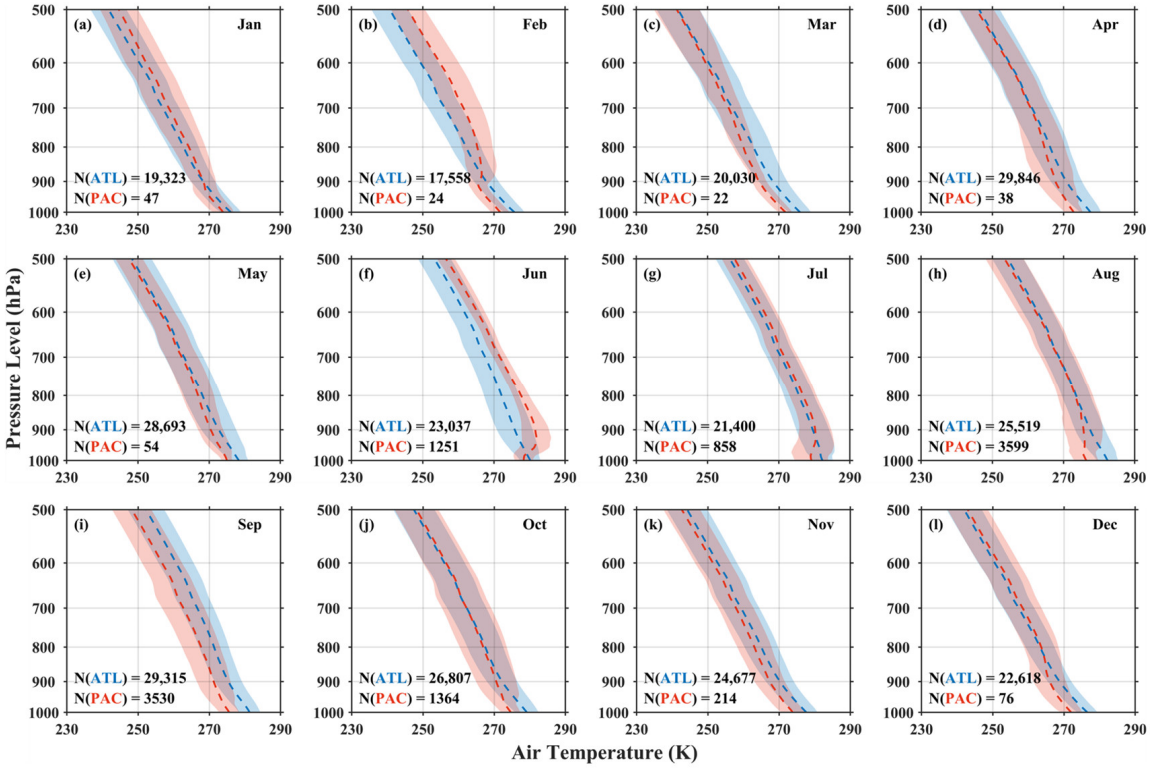


Figure 14. (**a**–**l**) Monthly distributions (mean ± 1 STD) of the MERRA-2 air temperature profiles beneath the 500 hPa level matched with the data in the MUDB at the Atlantic and Pacific Sectors of the Arctic. The number of each dataset is given in the lower left section of each panel.

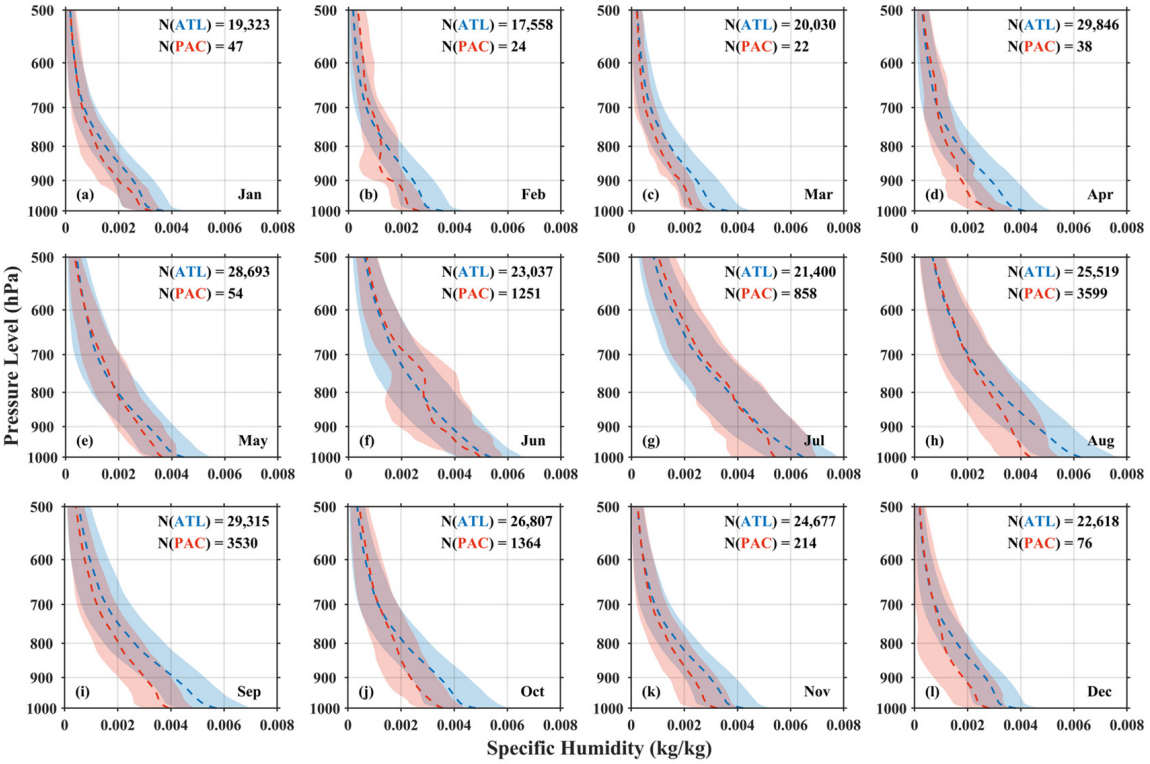


Figure 15. Similar to Figure 14a–l, but for the MERRA-2 specific humidity profiles beneath the 500 hPa level. The number of each dataset is given in the upper right section of each panel.

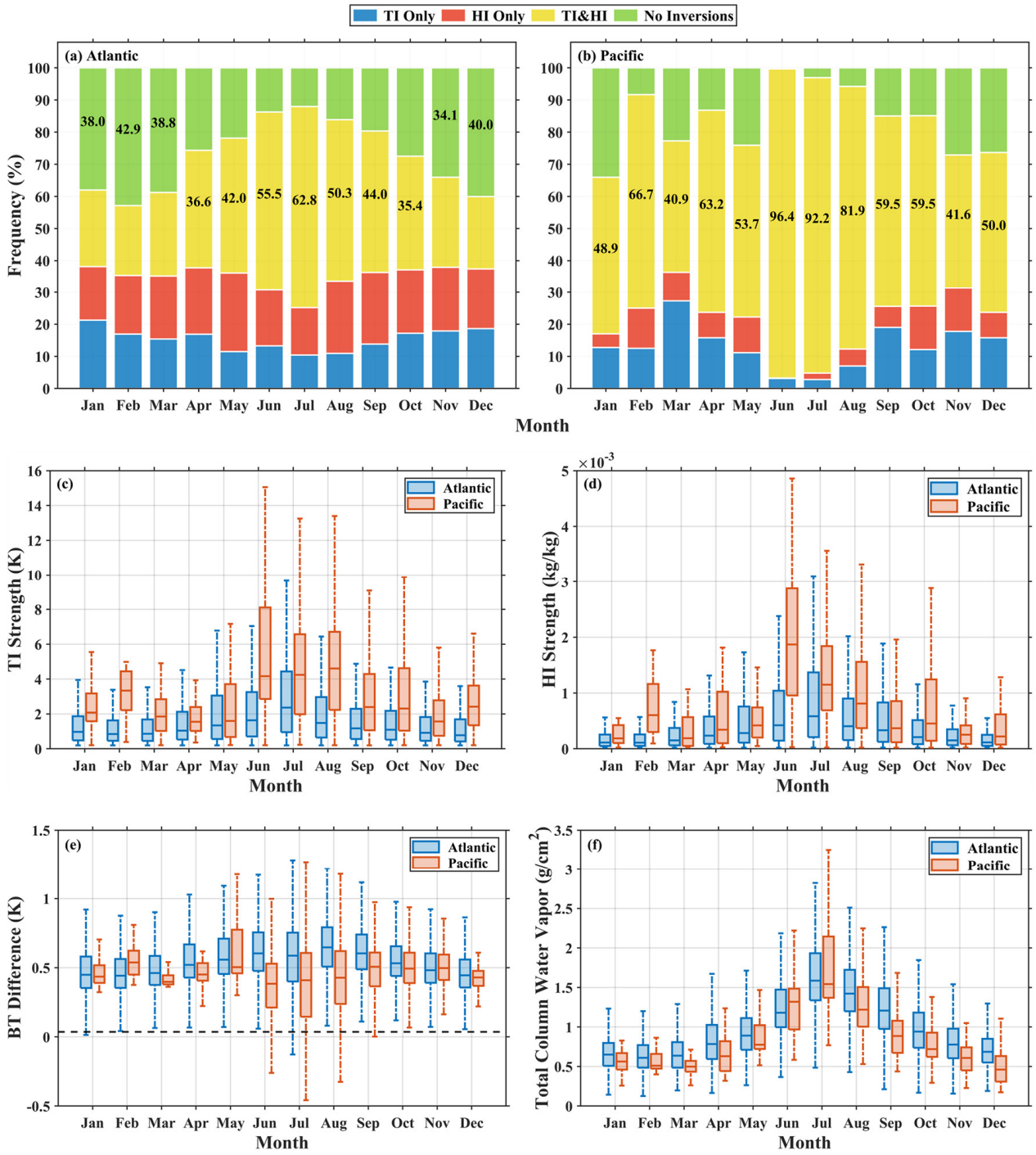


Figure 16. Monthly occurrence frequency of TI only (blue), HI only (red), simultaneous TI and HI (yellow), and neither TI nor HI (green) for the data in MUDB for the (**a**) Atlantic Sector and (**b**) Pacific Sector of the Arctic. The highest frequency among the inversion situations in each month is shown in the corresponding part of the column. Monthly variations of (**c**) TI strength and (**d**) HI strength for the Atlantic Sector (blue) and Pacific Sector (red) are plotted only when TI or HI exists. Monthly boxplots of (**e**) BT difference between 11 μm and 12 μm and (**f**) total column water vapor at the Atlantic side (blue) and Pacific side (red) are also given. The black dotted line in (**e**) is the horizon of 0.036 K. Outliers are not shown in the boxplots.

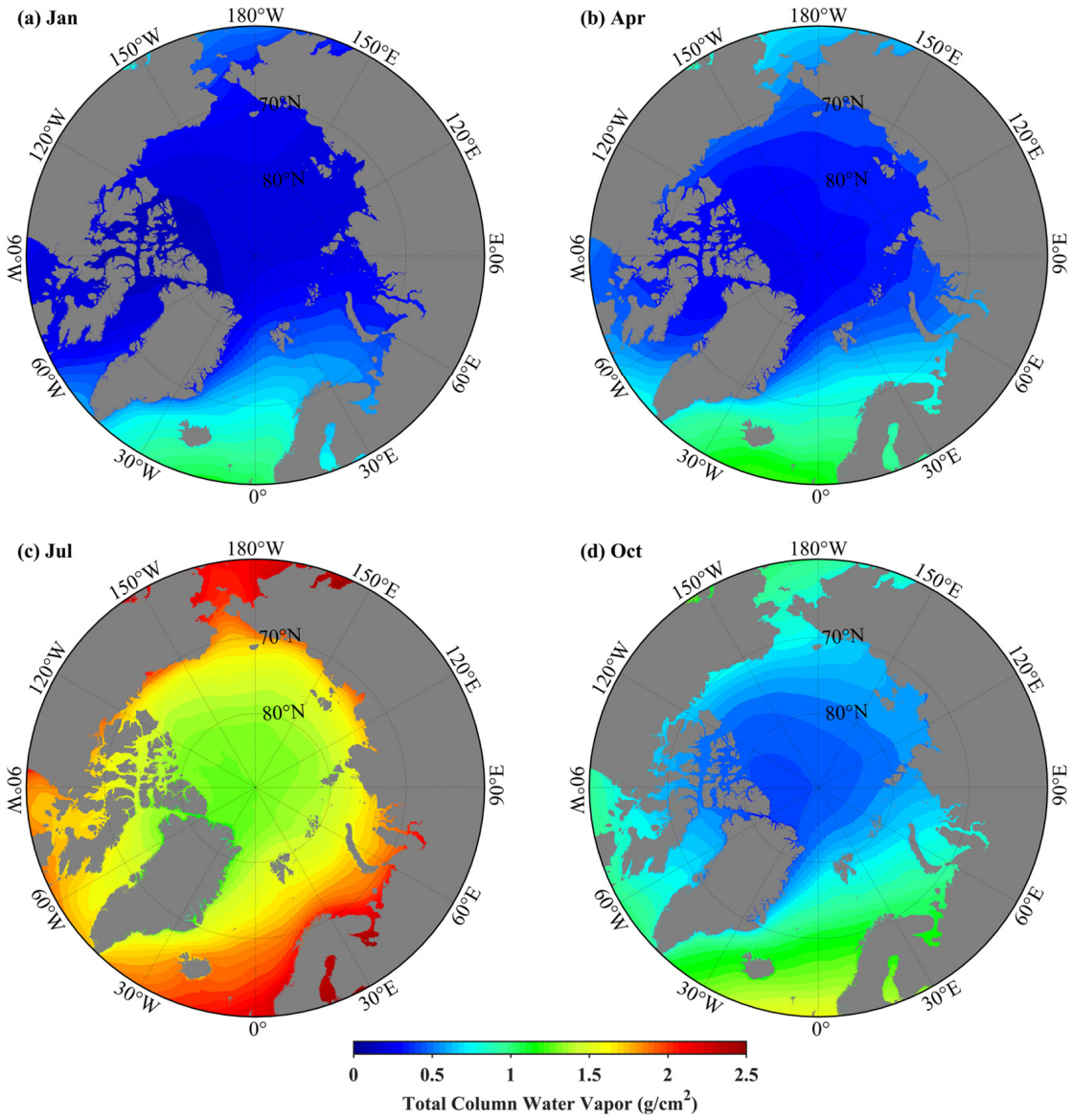


Figure 17. Maps of monthly MERRA-2 total column water vapor north of 60°N in (**a**) January, (**b**) April, (**c**) July, and (**d**) October. The data are averaged from 2002 to 2022.

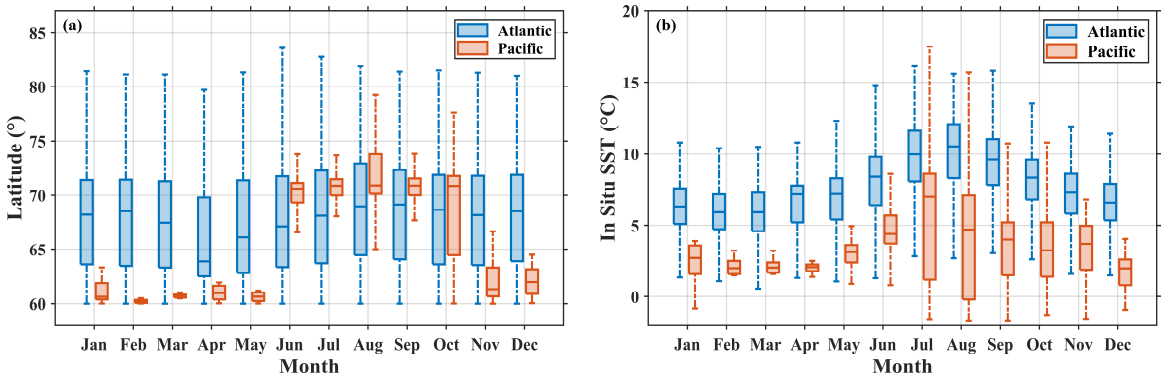


Figure 18. Monthly boxplots of (**a**) latitude of MODIS pixels and (**b**) in situ subsurface SST in the MUDB for the Atlantic (blue) and Pacific (red) Sectors. Outliers are not shown here.

6. Conclusions

The study reported here provides an overview of the characteristics of R2019 Aqua MODIS SST_{skin} retrievals at northern high latitudes above 60°N compared with collocated and simultaneous in situ buoy-measured SSTs from iQuam. The current MODIS R2019 SST_{skin} products have latitudinally and monthly dependent algorithm coefficients including a band north of 60°N to better represent Arctic atmospheres. The SST_{skin} biases compared to in situ measurements have a mean of −0.39 K for high-quality retrievals including both QL = 0 and QL = 1 data. This is more negative than the expected value of −0.17 K, indicating there is room for a further refinement of the atmospheric correction algorithm. The short time interval (within 30 min) between the MODIS and in situ observations in the MUDB should not introduce significant SST_{skin} errors, while the spatial difference (within 10 km) makes some contributions due to the potential effects of cloud contamination. By implementing the ADtree cloud classification scheme for R2019 reprocessing instead of the more conservative BDtrees algorithm applied in the previous R2014 version, the number of high-quality MODIS-iQuam matchups is increased markedly (by 63% in the period from 2013 to 2017), particularly during the day. Consequently, some anomalous 11 μm and 12 μm BT differences, not significantly > 0, are found in the MUDB, mostly in the daytime. These signals are very unlikely to be caused by undetected clouds due to the use of MODIS visible bands, but likely result from the existence of TI and HI in the lower troposphere. The occurrences of TI and HI are common in the Arctic, with ~60% in the MUDB, and are necessary but not sufficient for the identified BT difference anomalies, which are only 1.4% of the total valid data. The very strong coexisting TI and HI events tend to result in significant negative BT differences reaching −0.5 K. The more frequent anomalous BT differences observed in the warmer months can be attributed to the larger number of matchups as a result of there being more open water above 60°N and the better performance of the ADtree cloud mask in daylight. Such abnormal BT differences cause the retrieval algorithm to fail, resulting in large errors in MODIS SST_{skin} retrievals. Even for those significantly positive signals, their magnitude can be reduced by TI and HI events, leading to the water vapor effect being less represented in the atmospheric correction. By examining the two subregions of the Arctic, the Atlantic Sector and the Pacific Sector, large statistical discrepancies (0.4 K and 0.3 K for the mean and STD) in the MODIS ΔSST are present in the two sectors, associated with the different atmospheric conditions, including both temperature and humidity vertical profiles. More frequent and stronger TIs and HIs are found in the Pacific Arctic, particularly in the summer months. Also, considering the generally lower atmospheric water vapor content most of the time over the year, the resulting BT differences at 11 μm and 12 μm wavelengths are generally smaller than those in the Atlantic Arctic or are even negative. Essentially, the retrieval algorithm coefficients derived from the matchups mostly in the Atlantic Arctic are not appropriate for the atmospheric variability at the Pacific side, leading to large discrepancies in the error statistics.

Since the main causes of anomalous BT differences and the consequent different performances of the atmospheric correction algorithm at the Atlantic and Pacific sides of the Arctic have been revealed, the solutions for these two challenges are worth exploring in terms of algorithm refinement. In addition, R2019 processing of MODIS SST_{skin} data has not implemented the emissivity effect correction using the EΔBT index proposed by Jia and Minnett [27]; hence, its effectiveness should be verified, and the further optimization of this index is also necessary. Furthermore, the cool skin correction using the empirical estimate of an average value of −0.17 K in the constant coefficient of the MODIS SST_{skin} retrieval algorithm is seemingly inappropriate in the Arctic, possibly due to the generally greater surface net heat loss from the thermal skin layer into the atmosphere at high latitudes, or resulting from the localized wind speed distributions. It should be re-examined with more collections of simultaneous in situ SST_{skin} and subsurface SST measurements, especially at night or under high winds in the daytime.

Author Contributions: Conceptualization, C.J. and P.J.M.; Methodology, C.J. and P.J.M.; Software, C.J. and M.S.; Formal analysis, C.J.; Data curation, C.J. and M.S.; Writing—original draft, C.J.; Writing—review and editing, C.J., M.S. and P.J.M.; Visualization, C.J.; Supervision, P.J.M.; Project administration, P.J.M.; Funding acquisition, P.J.M. All authors have read and agreed to the published version of the manuscript.

Funding: This research was funded in part by a NASA contribution to the National Oceanographic Partnership Program (NOPP) Multi-sensor Improved Sea-Surface Temperature (MISST) project (the Lead PI at the outset was Chelle Gentemann, The Farallon Institute, with Peter Minnett as a Co-I) through contract 80NSSC20K0768 and by NASA grant 80NSSC21K1514, with Peter Minnett as the PI. Chong Jia was a University of Miami Graduate School Fellow.

Data Availability Statement: The MODIS matchups data base (MUDB) is available from https://seabass.gsfc.nasa.gov/archive/SSTVAL (accessed on 2 September 2024). The MERRA-2 reanalysis data are accessible from https://doi.org/10.5067/WWQSXQ8IVFW8 (accessed on 2 September 2024) and https://doi.org/10.5067/3Z173KIE2TPD (accessed on 2 September 2024).

Acknowledgments: The authors thank one of the reviewers who made many useful suggestions that have improved the clarity of the presentation.

Conflicts of Interest: The authors declare no conflict of interest.

References

1. Banzon, V.; Smith, T.M.; Chin, T.M.; Liu, C.; Hankins, W. A long-term record of blended satellite and in situ sea-surface temperature for climate monitoring, modeling and environmental studies. *Earth Syst. Sci. Data* **2016**, *8*, 165–176. [CrossRef]
2. Merchant, C.J.; Embury, O.; Bulgin, C.E.; Block, T.; Corlett, G.K.; Fiedler, E.; Good, S.A.; Mittaz, J.; Rayner, N.A.; Berry, D.; et al. Satellite-based time-series of sea-surface temperature since 1981 for climate applications. *Sci. Data* **2019**, *6*, 223. [CrossRef] [PubMed]
3. Ma, J.; Xie, S.-P. Regional Patterns of Sea Surface Temperature Change: A Source of Uncertainty in Future Projections of Precipitation and Atmospheric Circulation. *J. Clim.* **2013**, *26*, 2482–2501. [CrossRef]
4. Palmer, T.N.; Zhaobo, S. A modelling and observational study of the relationship between sea surface temperature in the North-West atlantic and the atmospheric general circulation. *Q. J. R. Meteorol. Soc.* **1985**, *111*, 947–975. [CrossRef]
5. Moron, V.; Gouirand, I.; Taylor, M. Weather types across the Caribbean basin and their relationship with rainfall and sea surface temperature. *Clim. Dyn.* **2016**, *47*, 601–621. [CrossRef]
6. Rasmusson, E.M.; Carpenter, T.H. Variations in Tropical Sea Surface Temperature and Surface Wind Fields Associated with the Southern Oscillation/El Niño. *Mon. Weather Rev.* **1982**, *110*, 354–384. [CrossRef]
7. Nobre, P.; Shukla, J. Variations of Sea Surface Temperature, Wind Stress, and Rainfall over the Tropical Atlantic and South America. *J. Clim.* **1996**, *9*, 2464–2479. [CrossRef]
8. Brander, K. Climate and current anthropogenic impacts on fisheries. *Clim. Chang.* **2013**, *119*, 9–21. [CrossRef]
9. Richardson, A.J.; Schoeman, D.S. Climate Impact on Plankton Ecosystems in the Northeast Atlantic. *Science* **2004**, *305*, 1609–1612. [CrossRef]
10. Jansen, E.; Christensen, J.H.; Dokken, T.; Nisancioglu, K.H.; Vinther, B.M.; Capron, E.; Guo, C.; Jensen, M.F.; Langen, P.L.; Pedersen, R.A.; et al. Past perspectives on the present era of abrupt Arctic climate change. *Nat. Clim. Chang.* **2020**, *10*, 714–721. [CrossRef]
11. Rantanen, M.; Karpechko, A.Y.; Lipponen, A.; Nordling, K.; Hyvärinen, O.; Ruosteenoja, K.; Vihma, T.; Laaksonen, A. The Arctic has warmed nearly four times faster than the globe since 1979. *Commun. Earth Environ.* **2022**, *3*, 168. [CrossRef]
12. Richter-Menge, J.; Druckenmiller, M.L.; Andersen, J.K.; Andreassen, L.M.; Baker, E.H.; Ballinger, T.J.; Berner, L.T.; Bernhard, G.H.; Bhatt, U.S.; Bjerke, J.W.; et al. The Arctic. *Bull. Am. Meteorol. Soc.* **2020**, *101*, S239–S286. [CrossRef]
13. Serreze, M.C.; Barrett, A.P.; Stroeve, J.C.; Kindig, D.N.; Holland, M.M. The emergence of surface-based Arctic amplification. *Cryosphere* **2009**, *3*, 11–19. [CrossRef]
14. Serreze, M.C.; Francis, J.A. The Arctic Amplification Debate. *Clim. Chang.* **2006**, *76*, 241–264. [CrossRef]
15. Cracknell, A.P. The advanced very high resolution radiometer (AVHRR). *Oceanogr. Lit. Rev.* **1997**, *44*, 526.
16. Minnett, P.J.; Evans, R.H.; Kearns, E.J.; Brown, O.B. Sea-surface temperature measured by the Moderate Resolution Imaging Spectroradiometer (MODIS). In Proceedings of the IEEE International Geoscience and Remote Sensing Symposium, Toronto, ON, Canada, 24–28 June 2002.
17. Coppo, P.; Ricciarelli, B.; Brandani, F.; Delderfield, J.; Ferlet, M.; Mutlow, C.; Munro, G.; Nightingale, T.; Smith, D.; Bianchi, S.; et al. SLSTR: A high accuracy dual scan temperature radiometer for sea and land surface monitoring from space. *J. Mod. Opt.* **2010**, *57*, 1815–1830. [CrossRef]
18. Minnett, P.J.; Kilpatrick, K.A.; Podestá, G.P.; Evans, R.H.; Szczodrak, M.D.; Izaguirre, M.A.; Williams, E.J.; Walsh, S.; Reynolds, R.M.; Bailey, S.W.; et al. Skin sea-surface temperature from VIIRS on Suomi-NPP—NASA continuity retrievals. *Remote Sens.* **2020**, *12*, 3369. [CrossRef]

19. Donlon, C.J.; Minnett, P.J.; Gentemann, C.; Nightingale, T.J.; Barton, I.J.; Ward, B.; Murray, M.J. Toward improved validation of satellite sea surface skin temperature measurements for climate research. *J. Clim.* **2002**, *15*, 353–369. [CrossRef]
20. Woodcock, A.H.; Stommel, H. Temperatures observed near the surface of a fresh-water pond at night. *J. Atmos. Sci.* **1947**, *4*, 102–103. [CrossRef]
21. Donlon, C.J.; Robinson, I.; Casey, K.S.; Vazquez-Cuervo, J.; Armstrong, E.; Arino, O.; Gentemann, C.; May, D.; LeBorgne, P.; Piollé, J.; et al. The global ocean data assimilation experiment high-resolution sea surface temperature pilot project. *Bull. Am. Meteorol. Soc.* **2007**, *88*, 1197–1214. [CrossRef]
22. Donlon, C.; Casey, K.; Gentemann, C.; LeBorgne, P.; Robinson, I.; Reynolds, R.; Merchant, C.; Llewellyn-Jones, D.; Minnett, P.; Piolle, J.-F.; et al. Successes and challenges for the modern sea surface temperature observing system. In Proceedings of the OceanObs'09: Sustained Ocean Observations and Information for Society, Venice, Italy, 21–25 September 2009; Volume 2. [CrossRef]
23. O'Carroll, A.G.; Armstrong, E.M.; Beggs, H.M.; Bouali, M.; Casey, K.S.; Corlett, G.K.; Dash, P.; Donlon, C.J.; Gentemann, C.L.; Høyer, J.L.; et al. Observational needs of sea surface temperature. *Front. Mar. Sci.* **2019**, *6*, 420. [CrossRef]
24. Castro, S.L.; Wick, G.A.; Steele, M. Validation of satellite sea surface temperature analyses in the Beaufort Sea using UpTempO buoys. *Remote Sens. Environ.* **2016**, *187*, 458–475. [CrossRef]
25. Donlon, C.J.; Martin, M.; Stark, J.; Roberts-Jones, J.; Fiedler, E.; Wimmer, W. The operational sea surface temperature and sea ice analysis (OSTIA) system. *Remote Sens. Environ.* **2012**, *116*, 140–158. [CrossRef]
26. Høyer, J.L.; Karagali, I.; Dybkjær, G.; Tonboe, R. Multi sensor validation and error characteristics of Arctic satellite sea surface temperature observations. *Remote Sens. Environ.* **2012**, *121*, 335–346. [CrossRef]
27. Jia, C.; Minnett, P.J. High latitude sea surface temperatures derived from MODIS infrared measurements. *Remote Sens. Environ.* **2020**, *251*, 112094. [CrossRef]
28. Minnett, P.J.; Alvera-Azcárate, A.; Chin, T.M.; Corlett, G.K.; Gentemann, C.L.; Karagali, I.; Li, X.; Marsouin, A.; Marullo, S.; Maturi, E.; et al. Half a century of satellite remote sensing of sea-surface temperature. *Remote Sens. Environ.* **2019**, *233*, 111366. [CrossRef]
29. Vincent, R.F.; Marsden, R.F.; Minnett, P.J.; Creber, K.A.M.; Buckley, J.R. Arctic waters and marginal ice zones: A composite Arctic sea surface temperature algorithm using satellite thermal data. *J. Geophys. Res. Ocean.* **2008**, *113*, C04021. [CrossRef]
30. Gentemann, C.L.; Minnett, P.J.; Steele, M.; Jenkins, R.; Cayula, J.F.; Castro, S.L.; Cornillon, P.; Robinson, D.H.; Harris, A.; Armstrong, E.M.; et al. Arctic MISST: Multi-sensor improved sea surface temperature: Continuing the GHRSST partnership and improving Arctic data. In Proceedings of the AGU Fall Meeting, Washington, DC, USA, 10–14 December 2018; p. A24K–11.
31. Jia, C.; Minnett, P.J. Ocean warm skin signals observed by Saildrone at high latitudes. *Geophys. Res. Lett.* **2023**, *50*, e2022GL102384. [CrossRef]
32. Jia, C.; Minnett, P.J.; Luo, B. Significant diurnal warming events observed by Saildrone at high latitudes. *J. Geophys. Res. Ocean.* **2023**, *128*, e2022JC019368. [CrossRef]
33. Jia, C.; Minnett, P.J.; Szczodrak, M. Assessment of Accuracy of Moderate-Resolution Imaging Spectroradiometer Sea Surface Temperature at High Latitudes Using Saildrone Data. *Remote Sens.* **2024**, *16*, 2008. [CrossRef]
34. Jia, C.; Minnett, P.J.; Szczodrak, M.; Izaguirre, M. High latitude sea surface skin temperatures derived from Saildrone infrared measurements. *IEEE Trans. Geosci. Remote Sens.* **2023**, *61*, 4200214. [CrossRef]
35. García-Mora, T.J.; Mas, J.-F.; Hinkley, E.A. Land cover mapping applications with MODIS: A literature review. *Int. J. Digit. Earth* **2012**, *5*, 63–87. [CrossRef]
36. Justice, C.O.; Townshend, J.R.G.; Vermote, E.F.; Masuoka, E.; Wolfe, R.E.; Saleous, N.; Roy, D.P.; Morisette, J.T. An overview of MODIS Land data processing and product status. *Remote Sens. Environ.* **2002**, *83*, 3–15. [CrossRef]
37. Esaias, W.E.; Abbott, M.R.; Barton, I.; Brown, O.B.; Campbell, J.W.; Carder, K.L.; Clark, D.K.; Evans, R.H.; Hoge, F.E.; Gordon, H.R.; et al. An overview of MODIS capabilities for ocean science observations. *IEEE Trans. Geosci. Remote Sens.* **1998**, *36*, 1250–1265. [CrossRef]
38. Wang, M.; Tang, J.; Shi, W. MODIS-derived ocean color products along the China east coastal region. *Geophys. Res. Lett.* **2007**, *34*, L06611. [CrossRef]
39. Hutchison, K.D. Applications of MODIS satellite data and products for monitoring air quality in the state of Texas. *Atmos. Environ.* **2003**, *37*, 2403–2412. [CrossRef]
40. King, M.D.; Menzel, W.P.; Kaufman, Y.J.; Tanre, D.; Bo-Cai, G.; Platnick, S.; Ackerman, S.A.; Remer, L.A.; Pincus, R.; Hubanks, P.A. Cloud and aerosol properties, precipitable water, and profiles of temperature and water vapor from MODIS. *IEEE Trans. Geosci. Remote Sens.* **2003**, *41*, 442–458. [CrossRef]
41. Kilpatrick, K.A.; Podestá, G.P.; Evans, R. Overview of the NOAA/NASA advanced very high resolution radiometer Pathfinder algorithm for sea surface temperature and associated matchup database. *J. Geophys. Res. Ocean.* **2001**, *106*, 9179–9197. [CrossRef]
42. Walton, C.C.; Pichel, W.G.; Sapper, J.F.; May, D.A. The development and operational application of nonlinear algorithms for the measurement of sea surface temperatures with the NOAA polar-orbiting environmental satellites. *J. Geophys. Res. Ocean.* **1998**, *103*, 27999–28012. [CrossRef]
43. Kilpatrick, K.A.; Podestá, G.; Walsh, S.; Williams, E.; Halliwell, V.; Szczodrak, M.; Brown, O.B.; Minnett, P.J.; Evans, R. A decade of sea surface temperature from MODIS. *Remote Sens. Environ.* **2015**, *165*, 27–41. [CrossRef]
44. Reynolds, R.W.; Smith, T.M.; Liu, C.; Chelton, D.B.; Casey, K.S.; Schlax, M.G. Daily high-resolution-blended analyses for sea surface temperature. *J. Clim.* **2007**, *20*, 5473–5496. [CrossRef]

45. Kilpatrick, K.A.; Podesta, G.; Walsh, S.; Evans, R.; Minnett, P. Implementation of version 6 AQUA and TERRA SST processing. *White Pap.* 2014. Available online: https://oceancolor.sci.gsfc.nasa.gov/reprocessing/r2014/sst/MODIS_V6_SST_changes.pdf (accessed on 2 September 2024).
46. Guenther, B.; Barnes, W.; Knight, E.; Barker, J.; Harnden, J.; Weber, R.; Roberto, M.; Godden, G.; Montgomery, H.; Abel, P. MODIS Calibration: A Brief Review of the Strategy for the At-Launch Calibration Approach. *J. Atmos. Ocean. Technol.* **1996**, *13*, 274–285. [CrossRef]
47. Brasnett, B. The impact of satellite retrievals in a global sea-surface-temperature analysis. *Q. J. R. Meteorol. Soc.* **2008**, *134*, 1745–1760. [CrossRef]
48. Liu, C.; Freeman, E.; Kent, E.C.; Huang, B.; Zhang, H.-M.; Berry, D.I.; Worley, S.J.; Ouellet, M.; Gaboury, I.; Ji, Z. ICOADS drifting buoy data recovery from BUFR and its impact on OISST and ERSST. In Proceedings of the Poster Presentation at 99th American Meteorological Society Annual Meeting, Phoenix, AZ, USA, 6–10 January 2019.
49. Brown, O.B.; Minnett, P.J.; Evans, R.; Kearns, E.; Kilpatrick, K.; Kumar, A.; Sikorski, R.; Závody, A. MODIS infrared sea surface temperature algorithm algorithm theoretical basis document version 2.0. *Univ. Miami* **1999**, *31*, 098-33.
50. Breiman, L.; Friedman, J.; Olshen, R.; Stone, C. *Classification and Regression Trees*, 1st ed.; Chapman and Hall/CRC: Boca Raton, FL, USA, 1984.
51. Kilpatrick, K.A.; Podestá, G.; Williams, E.; Walsh, S.; Minnett, P.J. Alternating decision trees for cloud masking in MODIS and VIIRS NASA sea surface temperature products. *J. Atmos. Ocean. Technol.* **2019**, *36*, 387–407. [CrossRef]
52. Freund, Y.; Mason, L. The alternating decision tree learning algorithm. In Proceedings of the 16th International Conference on Machine Learning, Bled, Slovenia, 27–30 June 1999; pp. 124–133.
53. Pfahringer, B.; Holmes, G.; Kirkby, R. Optimizing the induction of alternating decision trees. In Proceedings of the 5th Pacific-Asia Conference on Advances in Knowledge Discovery and Data Mining, Hong Kong, China, 16–18 April 2001; pp. 477–487.
54. Hollstein, A.; Segl, K.; Guanter, L.; Brell, M.; Enesco, M. Ready-to-Use Methods for the Detection of Clouds, Cirrus, Snow, Shadow, Water and Clear Sky Pixels in Sentinel-2 MSI Images. *Remote Sens.* **2016**, *8*, 666. [CrossRef]
55. Xu, F.; Ignatov, A. In situ SST quality monitor (iQuam). *J. Atmos. Ocean. Technol.* **2014**, *31*, 164–180. [CrossRef]
56. Gelaro, R.; McCarty, W.; Suárez, M.J.; Todling, R.; Molod, A.; Takacs, L.; Randles, C.A.; Darmenov, A.; Bosilovich, M.G.; Reichle, R.; et al. The modern-era retrospective analysis for research and applications, version 2 (MERRA-2). *J. Clim.* **2017**, *30*, 5419–5454. [CrossRef]
57. Putman, W.M.; Lin, S.-J. Finite-volume transport on various cubed-sphere grids. *J. Comput. Phys.* **2007**, *227*, 55–78. [CrossRef]
58. Han, Y.; Revercomb, H.; Cromp, M.; Gu, D.; Johnson, D.; Mooney, D.; Scott, D.; Strow, L.; Bingham, G.; Borg, L.; et al. Suomi NPP CrIS measurements, sensor data record algorithm, calibration and validation activities, and record data quality. *J. Geophys. Res. Atmos.* **2013**, *118*, 12734–712748. [CrossRef]
59. Kim, E.; Lyu, C.-H.J.; Anderson, K.; Vincent Leslie, R.; Blackwell, W.J. S-NPP ATMS instrument prelaunch and on-orbit performance evaluation. *J. Geophys. Res. Atmos.* **2014**, *119*, 5653–5670. [CrossRef]
60. Aminou, D. MSG's SEVIRI instrument. *ESA Bull.* **2002**, *111*. Available online: https://www.esa.int/esapub/bulletin/bullet111/chapter4_bul111.pdf (accessed on 2 September 2024).
61. Minnett, P.J. Consequences of sea surface temperature variability on the validation and applications of satellite measurements. *J. Geophys. Res. Ocean.* **1991**, *96*, 18475–18489. [CrossRef]
62. Schiermeier, Q. International Polar Year: In from the Cold. *Nature* **2009**, *457*, 1075–1077. [CrossRef]
63. Aktar, M.A.; Alam, M.M.; Al-Amin, A.Q. Global economic crisis, energy use, CO2 emissions, and policy roadmap amid COVID-19. *Sustain. Prod. Consum.* **2021**, *26*, 770–781. [CrossRef]
64. Shuvalova, J.; Chubarova, N.; Shatunova, M. Impact of cloud condensation nuclei reduction on cloud characteristics and solar radiation during COVID-19 lockdown 2020 in Moscow. *Atmosphere* **2022**, *13*, 1710. [CrossRef]
65. Yang, Y.; Ren, L.; Li, H.; Wang, H.; Wang, P.; Chen, L.; Yue, X.; Liao, H. Fast climate responses to aerosol emission reductions during the COVID-19 pandemic. *Geophys. Res. Lett.* **2020**, *47*, e2020GL089788. [CrossRef]
66. Meier, W.N.; Stroeve, J. An updated assessment of the changing arctic sea ice cover. *Oceanography* **2022**, *35*, 10–19. [CrossRef]
67. Embury, O.; Merchant, C.J.; Corlett, G.K. A reprocessing for climate of sea surface temperature from the along-track scanning radiometers: Initial validation, accounting for skin and diurnal variability effects. *Remote Sens. Environ.* **2012**, *116*, 62–78. [CrossRef]
68. Emery, W.J.; Yu, Y.; Wick, G.A.; Schluessel, P.; Reynolds, R.W. Correcting infrared satellite estimates of sea surface temperature for atmospheric water vapor attenuation. *J. Geophys. Res. Ocean.* **1994**, *99*, 5219–5236. [CrossRef]
69. Kumar, A.; Minnett, P.J.; Podestá, G.; Evans, R.H. Error characteristics of the atmospheric correction algorithms used in retrieval of sea surface temperatures from infrared satellite measurements: Global and regional aspects. *J. Atmos. Sci.* **2003**, *60*, 575–585. [CrossRef]
70. Minnett, P.J. A numerical study of the effects of anomalous North Atlantic atmospheric conditions on the infrared measurement of sea surface temperature from space. *J. Geophys. Res. Ocean.* **1986**, *91*, 8509–8521. [CrossRef]
71. Madhavan, S.; Xiong, X.; Wu, A.; Wenny, B.N.; Chiang, K.; Chen, N.; Wang, Z.; Li, Y. Noise characterization and performance of MODIS thermal emissive bands. *IEEE Trans. Geosci. Remote Sens.* **2016**, *54*, 3221–3234. [CrossRef] [PubMed]
72. Kahl, J.D.; Serreze, M.C.; Schnell, R.C. Tropospheric low-level temperature inversions in the Canadian Arctic. *Atmosphere* **1992**, *30*, 511–529. [CrossRef]

73. Naakka, T.; Nygård, T.; Vihma, T. Arctic humidity inversions: Climatology and processes. *J. Clim.* **2018**, *31*, 3765–3787. [CrossRef]
74. Palarz, A.; Daniel, C. Low-tropospheric humidity inversions over Europe: Spatiotemporal variability and relations to temperature inversions' occurrence. *Theor. Appl. Climatol.* **2020**, *141*, 967–978. [CrossRef]
75. Palo, T.; Vihma, T.; Jaagus, J.; Jakobson, E. Observations of temperature inversions over central Arctic sea ice in summer. *Q. J. R. Meteorol. Soc.* **2017**, *143*, 2741–2754. [CrossRef]
76. Vihma, T.; Kilpeläinen, T.; Manninen, M.; Sjöblom, A.; Jakobson, E.; Palo, T.; Jaagus, J.; Maturilli, M. Characteristics of temperature and humidity inversions and low-level jets over Svalbard Fjords in spring. *Adv. Meteor.* **2011**, *2011*, 486807. [CrossRef]
77. Zhang, Y.; Zhang, B.; Yang, N. Characteristics of temperature and humidity inversions based on high-resolution radiosonde observations at three Arctic stations. *J. Appl. Meteorol. Climatol.* **2022**, *61*, 415–428. [CrossRef]
78. Serreze, M.C.; Kahl, J.D.; Schnell, R.C. Low-level temperature inversions of the Eurasian Arctic and comparisons with Soviet drifting station data. *J. Clim.* **1992**, *5*, 615–629. [CrossRef]
79. Tjernström, M. Meteorological conditions in the central Arctic summer during the Arctic Summer Cloud Ocean Study (ASCOS). *Atmos. Chem. Phys.* **2012**, *12*, 6863–6889. [CrossRef]
80. Sotiropoulou, G. Atmospheric conditions during the Arctic Clouds in Summer Experiment (ACSE): Contrasting open water and sea ice surfaces during melt and freeze-up seasons. *J. Clim.* **2016**, *29*, 8721–8744. [CrossRef]
81. Jakobson, E.; Vihma, T. Atmospheric moisture budget in the Arctic based on the ERA-40 reanalysis. *Int. J. Climatol.* **2010**, *30*, 2175–2194. [CrossRef]
82. Nygård, T.; Graversen, R.G.; Uotila, P.; Naakka, T.; Vihma, T. Strong dependence of wintertime Arctic moisture and cloud distributions on atmospheric large-scale circulation. *J. Clim.* **2019**, *32*, 8771–8790. [CrossRef]
83. Jia, C.; Minnett, P.J. Effects of the Hunga Tonga-hunga Ha'apai eruption on MODIS-retrieved sea surface temperatures. *Geophys. Res. Lett.* **2023**, *50*, e2023GL104297. [CrossRef]
84. Woodgate, R.A.; Aagaard, K.; Weingartner, T.J. Monthly temperature, salinity, and transport variability of the Bering Strait through flow. *Geophys. Res. Lett.* **2005**, *32*, L04601. [CrossRef]

Disclaimer/Publisher's Note: The statements, opinions and data contained in all publications are solely those of the individual author(s) and contributor(s) and not of MDPI and/or the editor(s). MDPI and/or the editor(s) disclaim responsibility for any injury to people or property resulting from any ideas, methods, instructions or products referred to in the content.